Pilot scale Pyrolyser: Compliance and Mechanistic Modeling

A thesis presented in partial fulfillment of the requirement for the degree of

Master of Engineering

In

Chemical and Process Engineering

At Massey University, Palmerston North

New Zealand

Nadeem Salahaddin Abdul Caco

2017

Preface

A pyrolysis reactor was built in a previous project by Bridges et al (2013).The reactor is cylindrical in geometry, with a height of 1000 mm and an internal diameter of 750 mm, it stands vertically. There is a 900 mm tall and 100 mm in diameter perforated core in the center of the reactor. At the base, a combustion chamber provides the hot gases required for heating. The hot gases produced travel up and around the reactor through an annulus region of 11 mm. Heat from the gases is transferred to the reactor wall and then to the wood-chips inside. As drying and pyrolysis reactions occur, gases flow in the same direction as the heat towards the perforated core at the center. Hot pyrolysis gases then flow downwards towards the combustion chamber where they are partially combusted before flowing around the reactor and out the flue stack. This project aimed at mathematically modeling this reactor and also improving the way emissions are released so that it complies with EPA air quality standards.

A mathematical model of an 'open source' pilot-scale pyrolysis reactor was produced to predict the product yield, carbon foot-print, biochar quality and the time taken to achieve complete pyrolysis. A non-equilibrium thermodynamic approach was used which allowed for the use of COMSOL Multi-Physics to solve the model. The Finite Element Method (FEM) was used to solve the system of equations. Pyrolysis kinetics are complex and no single model has yet been widely accepted, therefore simplifications were necessary in this model so that a reasonable solution time could be achieved while producing acceptable results. The model profile of the centre temperature closely followed that of the experimental results and thus the model was considered valid.

In addition, modifications were made to the original design of the pyrolyser in order to improve emissions compliance and improve operations of the pyrolysis. It was important to manage fugitive emissions and completely combust any volatile vapours that would be released into the atmosphere while controlling the operating parameters. In order to achieve this, the following were implemented:

1) The combustion chamber was sealed completely so that no fugitive emissions can escape while limiting the ingress of oxygen.

2) A secondary blower was installed in order to better control the oxygen supply to the burners.
3) The original steel lid, which warped during pyrolysis runs resulting in gaseous leaks, was replaced with a more rigid ceramic lid that doesn't effectively expand when heated.
4) Two 3.4 kW burners were added to the single 3.4 kW burner flare. This gives a total power of 10.2 kW, which is estimated to be enough to completely burn all gaseous products leaving the system.

Acknowledgements

Firstly, I would like to express my gratitude to my supervisor Professor Jim Jones for offering me the opportunity to undertake this master's project and also for his immense patience and understanding, helpful criticism, advice and engagement throughout the project.

Furthermore, I would like to thank my secondary supervisor Dr. Georg Ripberger for all the time and energy he has invested which helped in the successful completion of the project.

I would also like to thank Professor John Bronlund for his advice and guidance and also for allowing me the use of his COMSOL Multi-Physics license, for which without the project would not have been possible.

Lastly, I would like to acknowledge the following people for their help and support throughout the duration of the project; Dr. Gonzalo Martinez Hermosilla, Mr. John Edwards and Mr. Ian Thomas.

Nomenclature

Symbol	Description	Unit	Typical Value
A	Pre-exponential factor	s^{-1}	-
a	Gas volume fraction	-	-
A,B,C	Constants used for calculation of thermal conductivity	W m^{-1} K^{-1}	-
A_l	Liquid contact area of sample	m^2	-
A_w	Water adsorption Coefficient	-	-
c	Concentration	mol m^{-3}	-
C_P	Specific heat	J kg^{-1} K^{-1}	-
C_{po}	Heat capacity of dry wood	kJ kg^{-1} K^{-1}	
c_{sat}	Saturated volumetric moisture content	%	-
D	Diffusivity co-efficient	m^2 s^{-1}	-
d	Diameter	m	-
ΔT	Temperature difference between the surface and hot gases (T_{ext}-T)	K	-
D_p	Particle diameter	m	
D_w	Water diffusivity	m^2 s^{-1}	-
E	Activation Energy	kJ mol^{-1}	-
F	Force	N	-
f_C	Fixed carbon content	wt. %	-
G	Specific gravity	-	1.54
g	Acceleration due to gravity	m s^{-2}	9.81
G_b	Specific gravity	-	-
h	Heat transfer coefficient	W m^{-2} s^{-1}	-
H	Enthalpy of reactions	kJ kg^{-1}	-
I	Identity matrix	-	-
J	Reaction rate	mol m^{-3} s^{-1}	
k	Kinetic constant	s^{-1}	-
K	Permeability	m^2	-
m	Mass	kg	-
M	Molecular weight	kg mol^{-1}	-
MC	Moisture content	wt. %	0-30%
MC_{fsp}	Moisture content at saturation	%	-
M_{fsp}	Fiber Saturation point	-	
M_i	Initial mass of sample	kg	-
M_t	mass of sample at time, t	kg	-
P	Pressure	Pa, kg m^{-1} s^{-2}	101325
Pr	Prandtl Number	-	-

Q	Heat generation	W m^{-3}	-
q	Heat flux	W m^{-2}	-
Q_{br}	Mass generation (adsorption/desorption)	kg m^{-3} s^{-1}	-
R	Ideal gas constant	J mol^{-1} K^{-1}	8.314
Ra	Rayleigh number	-	-
Re	Reynold's number	-	-
Sm	Shrinkage of wood	%	-
So	Shrinkage from wet wood to oven dry	%	-
T	Temperature	K	-
u	Darcy velocity	m s^{-1}	-
U	Averaged velocity	m s^{-1}	-
v	Rate of volatilisation	mol m^{-3} s^{-1}	-
VM	Volatile Matter	wt. %	-
x	Final moisture content of wood	%	-
y	Product yield	wt. %	-
y_{fc}	Fixed carbon yield	%	-

Greek Letters

∇	Differential operator given in Cartesian co-ordinates	-
Ω	Coefficient of thermal expansion	K^{-1}
α	Thermal diffusivity	m^2 s^{-1}
ε	emissivity	-
η	Reaction progress variable	-
κ	Thermal conductivity	W m^{-1} K^{-1}
μ	Dynamic Viscosity	Pa s
ρ	Density	kg m^{-3}
σ	Stefan-Boltzmann constant	5.67×10^{-8} W m^{-2} K^{-4}
τ	Turtuosity	-
φ	Porosity	-

Subscript

b	biomass
bed	packed bed of wood chips
c	char
conv	convection
eff	effective
ext	external

fiber	wood fiber
g	non-condensable gases
G	gas phase
i	species
in	inside
L	liquid phase
lw	liquid water
max	maximum
min	minimum
o	outside
P	particle
rs	surface-to-void radiation
rv	surface-to-surface radiation
T	tar
vw	water vapour
w	wood

Table of Contents

Figures

Tables

1. Literature review

1.1. Applications

The first use of charcoal was found in cave paintings some 30,000 years ago. By the year 3,750-3,500 BC it was being used by Egyptians, Sumerians, Europeans and Asians alike as a fuel source for cooking and as a reductant for the reduction of copper, zinc and tin ores in the production of bronze. Two thousand years later, the Egyptians began using charcoal for its medicinal properties. The Greek physician Hippocrates has been noted to use charcoal to treat various infections in 460 BC. Fast forward 40-50 years to 410 BC and charcoal has been reported to have been used as a construction material in wet areas that were prone to rotting, and in water and other liquid purification processes. By 1785, scientists had begun to systematically study the porous properties of charcoal. The Dutch chemist, Johann Tobias Lowitz has been credited for the discovery of charcoal's ability to remove colour from liquids, which led to its use in the sugarcane refining. Today, charcoal is still useful in a number of practices, from fuel for cooking, to metallurgical grade charcoal being used in the iron and steel smelters, to everything in between.

The future of charcoal use is still unclear. However, there are promising signs that show charcoal to be useful as a soil amender and as a method to sequester carbon dioxide, in order to mitigate both the emanating food shortage due to our depleting phosphorus reserves and the global warming disaster, fueled by the release of harmful amounts of greenhouse emissions such as CO_2 into the atmosphere. This is especially important for developing countries such as those in Africa and Asia where climate change and food shortages are already having an impact.

This project is motivated by sequestration, where biomass pyrolysis converts carbon from a liable to a stable form, thus almost permanently removing carbon from the atmosphere (Lehmann, 2007; Lehmann and Joseph, 2009). Char, the product of pyrolysis, is then stored in the soil. Desirable soil amendment properties which all contribute to improved water and nutrient retention. The cation exchange capacity (CEC) is a measure of a soil's ability to retain

cations for exchange with plants. This property has been shown to increase proportionately to the amount of organic matter in the soil, a property that can be influenced via the addition of biochar (The name given to charcoal which has been produced for the purposes of soil amendment and carbon sequestration from a renewable biomass feedstock) (Lehmann, 2007). Biochar has higher surface area, a more negatively charged surface and greater charge capacity than other organic matter, giving it a higher capacity to absorb cations per unit of carbon (Sombroek *et al.*, 2003; Laird *et al.*, 2010).

There have been some indications that it does benefit the soil and surrounding environment. Lehmann (2011) briefly reviewed this area and reported some interesting benefits of biochar interaction with soil biota. It was found that the high carbon content, nitrogen and minerals (ash) content of biochar helped stimulate microbial growth and diversity (O'Neill *et al.*, 2009). Depending on the mineral content and treatment temperature of biochar, it can also have beneficial effects due to the increase in pH levels and water retention capacity.

1.2. Physical and chemical characteristics of wood

There are two main groups of trees which are grown for their commercial value, as lumber, pulp and paper or for cellulose or lignin derived products:

1. Gymnosperms or softwoods (e.g. Pine)
2. Angiosperms or hardwoods (e.g. Oak)

Unlike other materials, such as plastics and metal alloys, which have very uniform properties due to their man-made nature, wood is an anisotropic, natural, porous material with variable thermal and physical properties, in the longitudinal, radial and tangential directions. Therefore, when studying wood pyrolysis, it is important to understand its many properties and its natural variability, so that processes which utilize wood can be optimized more easily.

2.2.1. Physical properties

The five distinct structural characteristics of a mature tree that can be observed with the naked eye when looking at the cross-section of a tree are: (1) outer bark, (2) inner bark, (3) softwood, (4) heartwood and (5) pith.

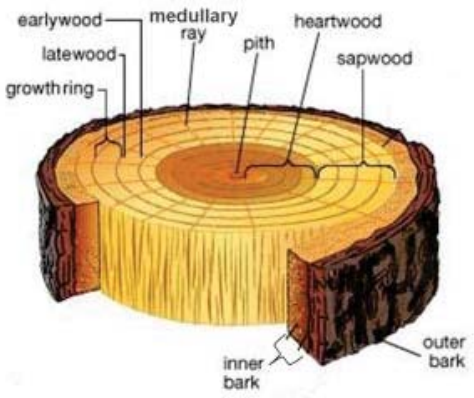

Figure 1-1: Physical structure of wood (Woodstairs, 2012)

The density of wood is affected by many growth factors including site, climate, species and irrigation/fertilization of the soil. During the early parts of the year (spring), wood grows at an increasingly faster rate compared to the later part (summer). As a result, the wood is lighter coloured with a lower density, followed by darker, denser wood, usually called summerwood (1). Fertilizers can also have a significant effect on density, usually lower density is observed in regions where fertilizers are applied to low nutrient soils (2). The types of fertilizers used, i.e., those containing phosphate or nitrogen, can also affect density in various ways. It is reported (Mcgrath, Copeland and Dumbrell, 2002) that nitrogen based fertilizers have a larger effect on the decrease in density compared to phosphate fertilizers. For simplicity, 440 kg m^{-3} is used for *Pinus radiata* pine (Richards, 2004). Other species of wood can range from 160 – 1,040 kg m^{-3} (Forest Products Laboratory, 2010).

2.2.2. Chemical properties

Wood is made up of three main chemical components: cellulose, hemicellulose and lignin - the rest of wood is made of extractives. They are highly complex macromolecular (high polymer) compounds which make up the cell wall.

Cellulose is the dominant component of all wood species; it makes up approximately 40-50% of wood by weight. It is a long chained, high molecular weight polymer made of D-glucose linked by β-1, 4-glycosidic bonds. Hydroxyl groups at different positions give cellulose its high chemical variability, due to their high donor reactivity. The hydroxyl groups are responsible for the high affinity of cellulose to adsorb water by means of hydrogen bonding (3).

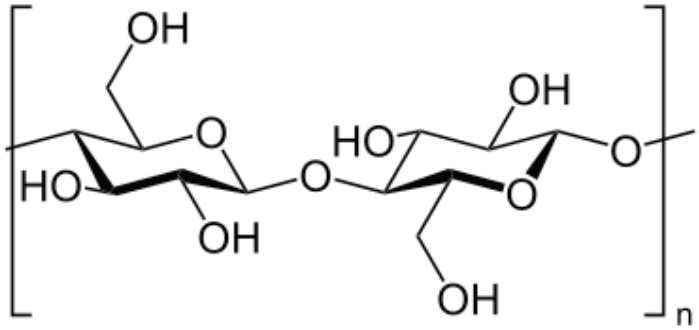

Figure 1-2: Structure of cellulose

Lignin makes up between 27-32% of wood and is the second largest constituent of wood, after cellulose. The chemical structure of lignin varies considerably. However, the main groups are phenyl propane building blocks, having phenolic hydroxyl groups in the para-position and methoxy groups in the meta-position (Pew, 1952). Hemicellulose, the third largest constituent in wood, is also a high molecular weight polymer similar to cellulose; however, it is made from sugars other than glucose. Extractives are the components in wood which give wood its identity, such as colour, odour, taste and preservation properties. The quantity of extractives in wood can vary from 1% up to 50%. They are termed extractives because they can be extracted using natural organic solvents and water. A combination of hydrocarbons, alcohols, aldehydes,

ketones, phenols, ethers, esters, lactones, oxides and acids make up extractives. In *Pinus radiata* the extractive content is 2-11 wt. % (Grønli, Várhegyi and Di Blasi, 2002).

2.2.3. Properties dependent on moisture content

The quantity of water (moisture content, MC) of wood can vary from as low as 5% to as high as 200% on a dry basis for fresh green wood (Forest Products Laboratory, 2010). Moisture can exist in wood in two forms: (1) ***free water*** which is liquid water or water vapour in cell lumina and cavities (pores) or (2) ***bound water*** held by intermolecular attraction, mainly hydrogen bonding within the cell walls. The physical and mechanical properties of wood vary based on the moisture content up to the fiber saturation point, after which the moisture content has no influence. The fiber saturation point M_{fsp} is the point at which the cell walls are completely saturated and no water exists in the cell lumina (pores) (Forest Products Laboratory, 2010). The point at which the cell walls and the pores are completely saturated is the maximum possible moisture content, MC_{max}. For any basic specific gravity, the MC_{max} can be estimated using equation 1 below:

$$MC_{max} = \frac{100(1.54 - G_b)}{1.54 G_b} \tag{1.1}$$

where G_b is the specific gravity on dry basis. For wood cell walls, the specific gravity is taken as 1.54. Water diffusivity, D_w is the measure of the rate of moisture flow through wood over unit thickness. D_w can be estimated using equation 2 below:

$$D_w \approx \left(\frac{A_w}{c_{sat}}\right)^2 \tag{1.2}$$

where c_{sat} is the saturated volumetric moisture content of the wood, and A_w, the water adsorption co-efficient is (Mukhopadhyaya *et al.*, 2002), estimated from:

$$A_w = \frac{M_t - M_i}{A\sqrt{t}} \quad (1.3)$$

where

M_t = mass of sample after time t, kg

M_i = Initial mass of sample, kg

A_l = liquid contact area of the sample, m^2

t = time taken for the specimen being measured to reach water saturation, s

Wood shrinkage can be estimated using equation 3 below:

$$S_m = S_o\left[1 - \frac{x}{MC_{fsp}}\right] \quad (1.4)$$

where S_o is the shrinkage percentage from wet wood to oven dry condition in the radial, tangential or volumetric direction. If MC_{fsp} is not known, then 30% MC can be assumed, and x is the final moisture content, this is defined as the fraction of water in the total weight of wood plus water (i.e. total mass). When the ring orientation of the wood is unknown or is a combination of tangential and radial (such as in wood chips), then the tangential value should be used.

2.2.4. Thermal properties

Thermal conductivity is a property of a material which defines its ability to conduct heat in a direction when subject to a heat flux (temperature difference). It is measured in W m^{-2} K^{-1} and is most commonly described by Fourier's law for heat conduction. Thermal conductivity of wood is affected by many factors, including: grain direction, physical irregularities such as checks and knots, extractive content, moisture content, density, fibril angle and temperature. Thermal conductivity is almost the same in the radial and tangential directions. However, it is

reported to be an average of 1.8 times faster along the grain. In relatively dry wood with a moisture content of less than 25%, thermal conductivity can be calculated using the following equation (Forest Products Laboratory, 2010):

$$\kappa = G_b(B + C \cdot MC) + A \quad (1.5)$$

Where, κ is the thermal conductivity in W m^{-1} K^{-1} and MC the moisture content (%) on a dry basis, G_b is the specific gravity on an oven dry basis. A, B and C are constants used when the G_b > 0.3 and MC < 25% :

A = 0.01864, B: 0.1941, C = 0.004064 (κ in W m^{-1} K^{-1}) (Forest Products Laboratory, 2010).

The heat capacity of wood depends on its moisture content and temperature and is independent of the wood species and density. The heat capacity of dry wood C_{po} (kJ kg^{-1} K^{-1}) can be calculated using the follow equation:

$$C_{po} = 0.1031 + 0.003867T \quad (1.6)$$

where $C_{P, \text{wet wood}}$ is determined by a simple mixture rule.

The measure of how quickly heat is conducted through a material in relation to its capacity to retain heat is called thermal diffusivity, α (m^2 s^{-1}). It is the ratio of material thermal conductivity to the product of density and heat capacity.

$$\alpha = \frac{\kappa}{\rho C_{P,wet\ wood}} \quad (1.7)$$

A common value of thermal diffusivity for wood is 1.6 x 10^{-7} m^2 s^{-1} (Forest Products Laboratory, 2010).

1.3. Pyrolysis

Wood pyrolysis is a complex process involving various chemical and physical phenomena. It includes heat transfer, water evaporation, primary and secondary decomposition reaction kinetics which are endothermic and exothermic, respectively, pressure build up and shrinkage. The result is the conversion of biomass, such as wood into three primary products, char, oil (tar) and non-condensable gases. The term biochar is used when referring to charcoal that is produced for the purpose of carbon sequestration as a soil amendment from a sustainable feedstock biomass (Lehmann and Joseph, 2009).

Pyrolysis of wood begins at approximately 200°C. It has been noted that hemicellulose begins to degrade at 220-315°C, cellulose at 315-400°C (Yang *et al.*, 2007), however lignin degrades over a much wider range of temperatures, from 200-500°C (Grønli, 1996). Pure lignin (brown alkali powder) has been shown to degrade over an even wider range of 160-900°C (Yang *et al.*, 2007). A number of factors play important roles in the concentration and quality of the end products of wood pyrolysis; these include feedstock (wood species), heating rates (°C min^{-1}), highest treatment temperature (HTT), particle size, residence time and moisture content. The most important of these are heating rate, HTT and residence time (Bridges, 2013).

Low-heating rates (referred to as slow pyrolysis) favour the production of char, while higher heating rates (fast pyrolysis) favour tar and non-condensable gas production (Chen, Zhou and Zhang, 2014). This work is focused on slow pyrolysis.

1.3.1. Pyrolysis gases

Pyrolysis gases are mainly comprised of CO_2, CO, CH_4, and lower amounts of H_2 and C_2 hydrocarbons (Scott, Piskorz and Radlein, 1985). The composition of liquid (tar) is highly dependent on the process environment, i.e., highest treatment temperature (HTT) and vapor-phase residence time. At temperatures of 773K or lower, primary tars are produced. Secondary

tars are produced at temperatures of 1123K and tertiary tars above 1123-1273K (Evans and Milne, 1987a, 1987b). The composition of tars increases in the order from low to high temperature of oxygenated compounds Phenolic esters>alkyl phenols>cyclic ethers>poly-aromatic hydrocarbons (PAHs)>Large PAHs.

1.3.2. Char properties & yield

The carbon content in char has a natural limit.It approaches an asymptote that is species dependent. As highest treatment temperature (HTT) is increased, the total carbon content decreases (as a fraction of the overall residual mass), and the higher the ash content (also as a fraction of total mass) becomes, as more carbon rich volatile components are driven off at higher temperatures. The ASTM D 1762-84 standard proximate analysis procedure, for char made from wood, states that biomass should be heated in a covered crucible to 950°C for 6 minutes and the weight loss recorded (Antal and Grønli, 2003). The weight loss measured is defined to be the volatile matter (VM) content (Grønli, 1996), and the residual solid is carbonized char

$$\%\, VM_{wood} = 100 * \left(\frac{m_{wood} - m_{cc}}{m_{wood}}\right) \tag{1.8}$$

where,

m_{char} = initial dry mass of wood, kg

m_{cc} = dry mass of carbonized char, kg

The carbonized char after the VM has been removed still contains some ash content, thus it is still not pure carbon. In order to determine the amount of ash in the char, the carbonized char (CC) is then heated in an open crucible to 750°C and maintained there for 6 hours until all the carbon has combusted. The remaining solid material is considered the ash content and is defined by equation 2 below (Grønli, 1996):

$$\% \, ash = 100 * \left(\frac{m_{ash}}{m_{dry \, wood}} \right) \quad (1.9)$$

where, m_{ash} = dry mass of solid that remains after combustion of the carbonized char (CC), kg

The fixed carbon content of the char is therefore:

$$\% \, fC = 100 - \% \, VM - \% \, ash \quad (1.10)$$

Most chars are produced at lower temperatures (300-600°C) than that used in proximate analysis. These chars all contain volatile matter (VM) to some extent. The VM content is used to determine char quality. Char with high VM content in the range of 20-30%, are mainly used for cooking whereas charcoal with lower VM in the range of 10-15% (or less) are considered metallurgical quality char. Bridges (2013) in her work was able to achieve VM content of less than 5%. Ash content is also used to determine char quality. Lower ash content of about 0.5% to 5% is an indicator of good quality char (Antal and Grønli, 2003), although in biochar applications, the effective fertiliser values depends on the amount and composition of the ash.

The char yield, $y_{char,}$ is an often cited quantity, given by the equation:

$$y_c = \frac{m_c}{m_{wood}} \quad (1.11)$$

where,

m_c = is the dry mass of char and, kg

m_{wood} = is the dry mass of the wood feedstock, kg

However, this method of calculating char yield gives no indication of the carbon content and thus the quality of char. A better method is to calculate the fixed-carbon yield.

$$y_{fC} = \frac{mass\ of\ fixed\ carbon}{mass\ of\ \ biomass\ on\ ash\ free\ basis} \tag{1.12}$$

$$y_{fC} = y_C * \left[\frac{\%\ fC}{100 - \%\ feed\ ash}\right] \tag{1.13}$$

where,

% feed ash = Percentage of ash content in the feedstock biomass.

Table 1-1 below shows the chemical composition of various organic feed stocks. The major difference is in the carbon content of the material with Rice hulls having the lowest at 52.61 wt. % while pine wood and macadamia nut shells both having the highest at 94.58 wt. %. Rice hulls also have a significantly higher ash content of 41.34 wt. % compared to the second highest of only 4.62 wt. %.

Table 1-1: Elemental composition of carbonized char for various feed-stocks (Antal and Grønli, 2003)

feed	C (wt %)	H (wt %)	O (wt %)	N (wt %)	S (wt %)	ash (wt %)
coconut shell	92.28	1.09	3.08	0.47	0.04	2.78
corncob	86.38	1.20	5.34	0.56	0.05	4.31
kukui nut shell	90.31	1.03	4.31	0.42	0.02	3.27
leucaena wood	85.41	1.27	6.37	0.53	0.04	4.62
macadamia nut shell	94.58	0.97	2.93	0.47	0.03	1.04
oak board	91.50	1.22	3.55	0.18	0.01	1.04
oak slabs	92.84	1.09	3.49	0.24	0.04	1.46
pine wood	94.58	1.06	3.09	0.11	0.04	0.69
rice hulls	52.61	0.82	3.87	0.57	0.06	41.34

1.3.3. Inorganic material (Ash)

High amounts of inorganic matter (ash) in biomass such as potassium can have adverse effects on the thermal conversion processes, such as fouling, slagging and, in the case of fluidized bed reactors, bed agglomeration (Dayton *et al.*, 1999). The inorganic content can also catalyse the reactions, driving them towards higher char yield (Georg, 2016)

1.4. Previous pyrolysis modeling work

The efficient design and optimization of pyrolysis reactors can be first validated then used predictively by building sophisticated mathematical models to simulate the pyrolysis mechanisms along with the various physical phenomena associated with pyrolysis, such as heat and mass transfer. A considerable amount of analytical and theoretical data has been collected over the past 60-70 years in the field of pyrolysis, which has resulted in numerous kinetic and mechanistic models ranging from very basic to very complex and detailed. They are broadly discussed below.

1.4.1. Overview

Early pyrolysis model like that developed by Bamford et al. (1946) are based on the following assumptions:

1) One-dimensional heat and mass transfer.
2) Only conductive heat transfer within the solid particle.
3) Re-condensation of volatile products (including water) is neglected.
4) Char shrinkage is neglected.
5) Wood is a homogeneous solid.
6) Wood is dry and no free-water is available.

One of the most comprehensive pyrolysis models was put forward by Shafizadeh and Chin (Shafizadeh and Chin, 1977) who focused on the decomposition kinetics when analysing the thermal behavior of cottonwood, concluding that the thermal behavior of wood is the sum of its three main components: cellulose, hemicellulose and lignin. The products of pyrolysis identified were char, tar and gas. Shafizadeh and Chin (Shafizadeh and Chin, 1977) also pyrolysed the components separately to measure their contribution to the final product yields. For example, cellulose was found to be the major contributor towards the volatile products (tar and gas), while lignin contributed more towards the char yield. The products of the individual pyrolysed components also seemed to add-up to the yields from the pyrolysis of wood, suggesting that there is very little to no interaction between the components during pyrolysis. Figure 1.3 shows this proposed kinetic model. Although Shafizadeh and Chin (Shafizadeh and Chin, 1977) did mention that further heating of the volatiles will result in the formation of secondary gas and char, no kinetic model for this reaction pathway was proposed. This model has served as the basis for almost all pyrolysis models and studies since.

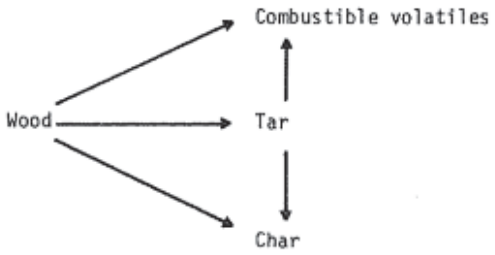

Figure 1-3: Kinetic model proposed by Shafizadeh and Chin in (Shafizadeh and Chin, 1977)

In the recent past, various pyrolysis models have been presented by a number of authors (Di Blasi, 1996; Grønli, 1996; Bellais, 2007; J. Ratte *et al.*, 2009; Park, Atreya and Baum, 2009; Lam, Oyedun and Hui, 2012) that have both included the mechanism of Shafizadeh & Chin (Shafizadeh and Chin, 1977) and have managed to remove some of the assumptions originally proposed by Bamford (1946). All these models take into account the diffusion of gaseous products through the particle which is commonly described by Darcy's Law of fluid flow in porous media. Some have also included shrinkage in their models (e.g., Hagge and Bryden, 2002).

1.4.2. Drying of wet wood particles

Experimentally, it has been shown that when studying heating as a function of time during pyrolysis of large wood particles, a plateau of temperature is observed at about 100°C. The duration of the plateau is proportional to the moisture content. It is termed the drying plateau, and is considered to start at about 80°C and end at 120°C. Modeling the drying process is therefore important as it can have a significant impact on temperature prediction, especially in systems containing many particles.

Researchers have developed a number of ways to numerically model the drying regime of wood when subject to heat, such as during pyrolysis, combustion or even low temperature drying of biomass, <200°C. Krieger Brockett et al. (4) treat drying as an additional decomposition reaction with an Arrhenius expression. This technique has two advantages: (1) it includes an activation energy, which accounts both a temperature dependent evaporation rate and the fluctuations in strength of bound water, (2) it has numerical stability in a code that handles many of these Arrhenius expressions. It also has its disadvantages due to the experimentally derived nature of the exponents in the Arrhenius expression. To get around this Bruchmuller et al. (2011) treated drying as a boiling process around the temperature of 100°C, by balancing the energy required for water vaporization and the energy absorbed by the particle from the surroundings. When $T > T_{vaporization}$ then drying took place, until either $T < T_{vaporization}$ or the mass of water available was consumed. This method includes a Dirac function[1], making the function stiff[2], and so appropriate techniques must be employed in order to deal with it.

1.4.3. Pyrolysis chemical reaction kinetics

Degradation of biomass kinetics is studied either isothermally or non-isothermally. During the isothermal analysis, biomass is placed in a heated chamber which is set at a constant temperature and the sample weight change is recorded as a function of either temperature or

[1] A Dirac function has the value 0 for all $x \neq 0$ and ∞ for $x = 0$.

[2] In Mathematics, a stiff equation is a differential equation for which some terms can lead to very rapid variation in the solution, making it unstable, unless a very small step size is taken.

time. During non-isothermal analysis, the temperature in the chamber increases with time based on an assigned heating rate. The methods are used to determine Arrhenius Kinetic parameters.

Although there have been a large number of experimental studies, there is still no universally accepted model that can predict the pyrolysis rate and provide *a priori* knowledge about the final decomposition over a wide range of parameters, such as particle size. Most kinetic studies are conducted using Thermo-gravimetric Analysis (TGA) because the mass of the sample is the most convenient property in the study of global chemical kinetics (Mamleev, Bourbigot and Yvon, 2007).

Di Blasi C (1993, 2008) suggested various classes of mechanisms for wood pyrolysis. The models are categorized into three distinct classes: (1) one-step global model; (2) one-step multi-reaction models and; (3) two-step semi global model. One step global model considers pyrolysis (first explored by Bramford et al. 1946) as a single step first order reaction of the following form:

$$\frac{dY}{dt} = -kY \tag{1.14}$$

where,

k = Kinetic constant = $Ae^{\left(\frac{-E}{RT}\right)}$

A = pre-exponential rate constant (s^{-1})

E = Activation energy (kJ mol^{-1})

R = Ideal gas constant = 8.314 (J mol^{-1} K^{-1})

The one-step multi reaction model (Class (2)) considers those pyrolysis reaction mechanisms which involve simultaneous and competing first order reactions, in which wood decomposes to

produce the various different primary pyrolysis products, i.e. char, tar and oil (following the mechanism proposed by (Shafizadeh and Chin, 1977)

$$\text{Wood} \rightarrow (\text{Volatiles} + \text{gas})_1$$
$$\text{Wood} \rightarrow (\text{Char})_1$$

While this reaction mechanism accounts for multiple products of pyrolysis of wood, it neglects to include the effects of secondary reactions and the vapour phase residence time. This is accounted for in two-step semi global models (class 3) which are two-step reactions in which the pyrolysis products of the primary reactions further decompose to produce secondary products.

$$\left.\begin{array}{l}\text{Wood} \rightarrow (\text{Volatiles} + \text{gas})_1 \\ \text{Wood} \rightarrow (\text{Char})_1\end{array}\right\} \text{Primary Reactions}$$

$$(\text{Volatiles} + \text{Gases})_1 + (\text{Char})_1 \rightarrow (\text{Volatiles} + \text{Gases})_2 \text{ Secondary Reactions}$$

By including the secondary reactions in the kinetic scheme, the product yields become a function of not only temperature, but also vapour-phase residence time and heating rate. Secondary tar reactions can occur at sufficiently high temperatures and given enough vapour phase residence time. They are classified as both homogeneous, when in the vapour phase and heterogeneous when interacting with the char surface or when moving inside the char particle. Cracking, re-polymerization, condensation and partial oxidation are all processes which can occur during secondary reactions (Morf, Hasler and Nussbaumer, 2002). This scheme may provide accurate results for the modeling of very small, single particles, however it does not accurately describe the mechanisms at play on a larger, multi particle system. In these the structure and size of the particles affects the residence time where the volatiles interact with the char as they move along the pressure gradient and escape into the surrounding void

volume. Accounting for such effects is extremely difficult. The approach needed is to experimentally determine the kinetic parameters for each system (geometry, particle size, heating rate).

Fantozzi et al (2007) used the principles of the third class model suggested by Di Blasi (Di Blasi, 1996) to model a rotary kiln pyrolysis reactor. According to Di Blasi (Di Blasi, 1996), as heat is provided, wood undergoes primary endothermic reactions according to the scheme shown in figure 1.4 below, resulting in the production of gas_1, tar_1 and $char_1$. If the reaction is then allowed to continue to reach higher temperatures and allow for enough vapour phase residence time of the tar_1, then it will decompose further to produce permanent gas_2 and $char_2$.

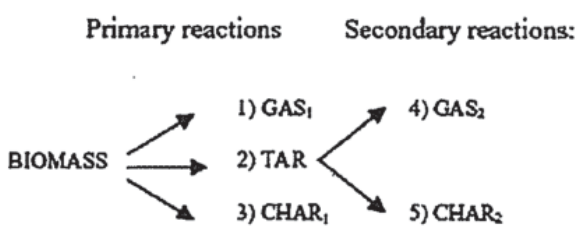

Figure 1-4: Simplified scheme for biomass pyrolysis as derived from (Di Blasi, 1996)

In the work by Fantozzi et al. (2007), a model was developed using this scheme to simulate the change in product yields with respect to moisture content, rotational speed of the rotary kiln drum and density of the wood chips. However, this work does not use a rotary kiln, but instead a vertical fixed bed heated from below and from the side, with pyrolysis gas convection from a central perforated core.

1.4.4. Numerical methods

There are generally two main numerical methods that can be used to approximate boundary condition problems.

1. Finite Difference Method (FDM).
2. Finite Element Method (FEM).

The FDM has been used by the majority of researchers so far who have attempted to model the pyrolysis process (Di Blasi, 1993; Grønli, 1996). When using the finite differencing method to solve numerically, the solution to the partial equation is approximated by some difference function. A difference function is that which is defined only at a finite number of points (grids) on the domain and boundary.

The finite element method is a numerical technique used to solve boundary value problems for partial differential equations (PDEs) and Ordinary Differential Equations (ODEs), by dividing the problem into small discretized parts, known as finite elements. Ratte et al. (2009) has used this method to model the pyrolysis of a single wood particle.

2. Reactor design & compliance

The pyrolysis reactor used for this modeling and optimization project was that described by Bridges, et al. (2013), shown below (figure 2.1). It was designed and built with the purpose of investigating the viability of small scale, mobile pyrolysis units.

Figure 2-1: Batch pyrolysis reactor designed and built by Bridges (2013) **during a run with 70 kg of wood chips.**

The reactor is a steel drum of height 1000 mm and radius of 375 mm. A combustion chamber sitting underneath supplies the heat for the pyrolysis process via LPG combustion. The heated gases from the combustion chamber travel through an annular region around the outside of the reacting chamber and out through a flue stack. A side view schematic is shown in figure 2-2.

Once the chamber is heated, drying of the wood chips begins, followed by pyrolysis, which produces water vapour and hydrocarbons (tar and non-condensable gases). These flow from

the outer region of the reactor chamber towards the central perforated core, after which they flow down into the combustion chamber, where the volatiles are partially combusted to provide heat for the process. The mixture of partially combusted gases flow through the annular zone and out the flue stack. Previously there was a forced draft 3 kW burner at the top of the stackthat was used to ignite these gases as they mixed with air. The purpose of this flare was to reduce particulate and greenhouse gas emissions. However, it was later discovered that this system was insufficient at completely combusting the gases and thus needed to be modified in order to comply with air quality standards. The following two sections discuss the original flare and then the redesign.

2.1. Original flare system

The reactor system has been designed (see Bridges, 2013) to avoid the possibility of overheating which can cause catastrophic meltdown. To do this the combustion zone must be partially starved of air so that excessive combustion cannot occur during the heating phase between ~280-450°C when most pyrolysis gases are produced. An inherently safe design was required. The peak allowable temperature is defined by the material of construction.

The reactor is built out of stainless steel 304, which is rated to a maximum operating temperature of 1050°C. This temperature can easily be exceeded if all the pyrolysis gases are combusted in the combustion chamber. Therefore, the flue stack was designed to be 80 mm in diameter and 2.5 m tall in order to limit the draft air supply coming into the combustion chamber via the secondary gas holes at the base of the combustion chamber. Also the main 26 kW burner and its forced draft air supply is turned off during peak pyrolysis gas production, which starts when the centre temperature exceeds 340°C. This means only the secondary 3 kW burner partially combusts the pyrolysis gases. Therefore, in order to emit ‘clean’ gases, a flare is required at the top of the flue stack to completely combust the pyrolysis gases.

Figure 2.2 above shows the schematic of the original flare system. In order to achieve complete combustion of particulate and other products of incomplete combustion, the flare zone needs to be maintained at 850-1200°C, and the gases given at least 0.3 seconds of residence time in the combustion zone (Caine, 2000). If the temperature is below this range, then complete combustion does not occur and a large amount of carbon monoxide and methane is released into the atmosphere. On the other hand, if it is too high (>1200°), then there is a risk of producing dioxins, furans, poly-aromatic hydrocarbons (PAHs) and NO_x. Indeed, PAHs are increasingly produced at above 350°C, especially in low oxygen conditions (Abdel-Shafy and Mansour, 2015).

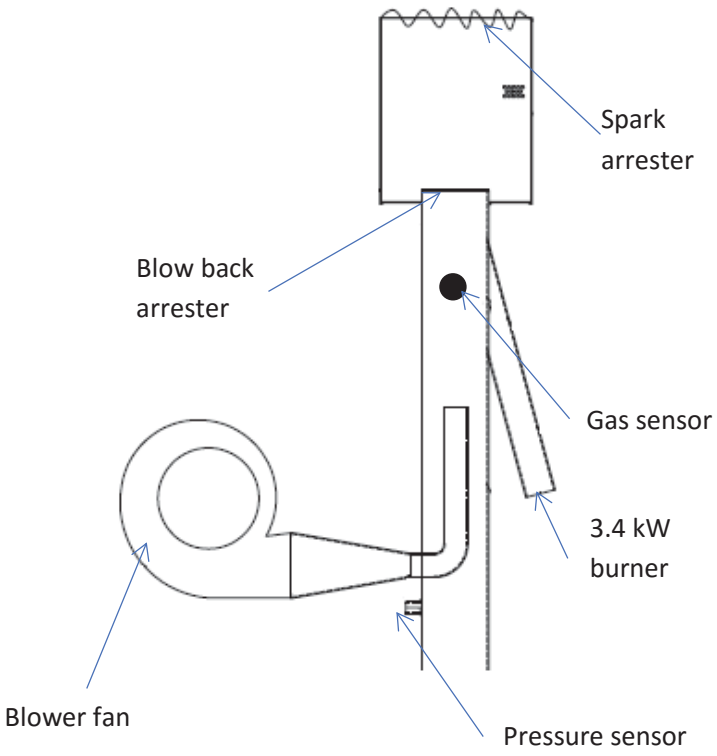

Figure 2-2: Schematic of the original flare

This flare was intended to ignite the combined flow of the combustion gases and the pyrolysis gases. However, the poor flammability of this mixture had not been considered. Flammability is

poor due to the high proportion of inert gases such as N_2, CO_2 and H_2O. The nitrogen gas enters with the air to the forced draft burners and via the secondary air inlets depending on the updraft. Water vapour and carbon dioxide are combustion and pyrolysis reaction products, water is also present depending on the moisture content of the biomass. All of these suppress the flammability, which then depends on the concentration and ignition characteristics of CO, CH_4, H_2 and other hydrocarbons present in the gas stream. Within the flue gas, the concentrations of flammable gases CO, H_2, and CH_4 vary with temperature and time. The Kinetics and indeed the concentration profile is not well known even in systems where no air is present for partial combustion. It is likely that some of the concentrations of CO, H_2 and CH_4 are below the lower flammability limits (See Table 2-1). Also reducing the flammability is the relatively low heat of combustion of CO which is likely to be the flammable substance present in the highest concentration. Although averaged over 30 minutes, during peak gas evolution period of 340-450°C Figure 2.3 shows that the flue concentration of CO was 10,000 ppm or 1% vol.

Table 2-1: Auto-ignition temperatures of the flammable gases found in the pyrolysis flue stream. Gas concentrations below the lower limit are too lean to ignite and gas concentrations in the upper limit are too rich (*NIST Chemistry WebBook*, 2016)**.**

Normal Atm. Auto Ignition Temperature (°C)	Species in air	Concentration (%)		$\Delta h_c\ (MJ\ kg^{-1})$
		Lower	Upper	
500-571	H_2	4	75	143
580	CH_4	5	15	55
609	CO	12	75	10

Therefore, to ensure complete combustion (800-1200 °C for > 0.3 seconds), a secondary firing system is needed. This system must meet environmental emissions standards.

Although there are no specific emissions limits for pyrolysis, the United States of America Environmental Protection Agency (EPA) does have a number of limits which vary depending on the energy output of the reactor, type of fuel and reactor configuration. The most lenient of

these is a stack concentration limit of 2400 ppm carbon monoxide at a minimum of 1-hour sampling time for a biomass suspension burner exceeding 3 MW of heat production. Figure 2.3 below clearly shows that this reactor with the original flare system exceeds this limit by seven times. However, while the stack emissions were excessive, the working environment for the operators was still safe, an environmental carbon monoxide meter was used and the levels never exceeded 50 ppm, which is within the 1 hour work safe limit Table 2-1 (WorkSafe, 2016).

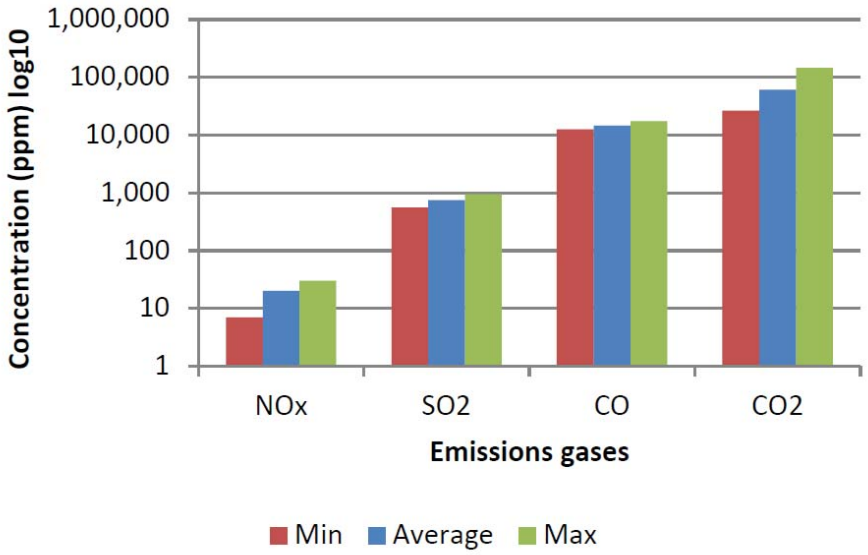

Figure 2-3: Flue gas emissions concentrations from the Pyrolysis reactor.

Table 2-2: Short-term New Zealand work place CO exposure limits

CONCENTRATION (ppm)	EXPOSURE PERIOD
200 ppm	15 minutes
100 ppm	30 minutes
50 ppm	60 minutes

2.2. New flare design and operation

The pyrolyser shown on the next page (Figure 2.4) was designed and built for the purpose of producing high quality biochar. It is capable of processing 60-70kgs of wood-chips (ρ_{pine} = 480 kg m^{-3}). Once loaded, the process begins by heating the inner reactor. The heat is initially supplied by a 26 kW and a 3.4 kW burner which both run off LPG. This is done until the core of the reactor has reached 340°C, after which the 26 kW burner is automatically turned off and only the 3.4 kW burner is left on. At 340°C, pyrolysis reactions are well under-way, producing volatile hydrocarbons (and moisture in the form of water vapour) which move towards the centre of the inner reactor and down the perforated core, into the combustion chamber. Some of these gases are ignited in the combustion chamber by the 3.4 kW burner. The CO_2, moisture and un-combusted hydrocarbons then travel up the drum annulus and out the flue stack at a peak velocity of 1.2 m s^{-1}, where they are flared. To pass US & NZ EPA air quality guidelines, the gases and particulate must fully combust before being released into the atmosphere. This required the redesign of the flare.

In order to achieve complete combustion a temperature of 800-1200 °C must be maintained in the combustion zone of the flare where the gases have a residence time of no less than 0.3 seconds. Two 3.4 kW burners were determined as sufficient to achieve this even when there are no or very little volatiles coming through, for example during the initial pyrolysis stage. For the purpose of safety, flame detectors were also installed in order to ensure that gas does not flow without flame. The position of the burners was also moved closer to the tip of the flue stack; to allow for better mixing with ambient air. A windshield was also added to retain the heat and provide height to ensure enough residence time for the flue gases. The burners were positioned at 120° from each other (Figure 2.5) and at an angle of 10° relative to the flue stack so that they are pointing inwards so that all three flames contact at the very tip, creating one large central flame (Figure 2.6). In this way, bypassing of incompletely combusted gases is avoided. Furthermore the top of the combined flame is directed onto a central wire mesh ball which acts as a heat sink, to re disperse radiant heat and to provide turbulent mixing.

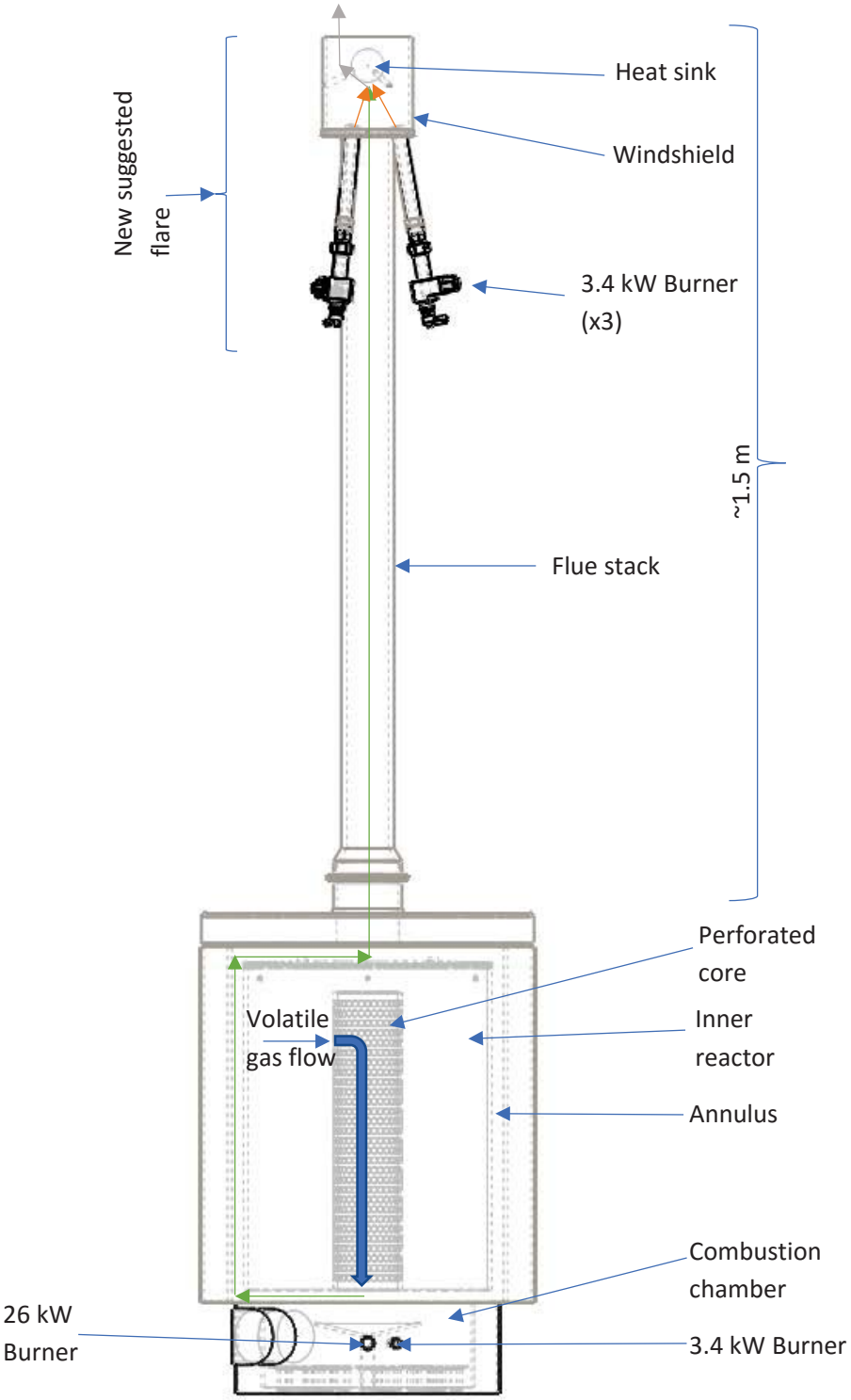

Figure 2-4: Schematic of the pyrolysis system with the new flare

Figure 2-5: Plan view of the flare showing the angle of the burners, arranged in a triangular pattern around the flue stack

Figure 2-6: Elevation view of the flare showing the angle of burners relative to flue stack

2.3. Fugitive emissions

The original lid (Figure 2.7) warped during pyrolyser operation leading to fugitive emissions. The lid was made from sheet stainless steel 304 with a layer of insulation in the centre. During heating, the bottom of the lid expanded to a greater extent than top side because the insulation layer kept the top side cool. The different expansion rates, caused the lid to bow and warp, the analogy is an uneven wok. This created openings around the perimeter of the reactor, allowing either volatile pyrolysis vapours to escape or the ingress of air.

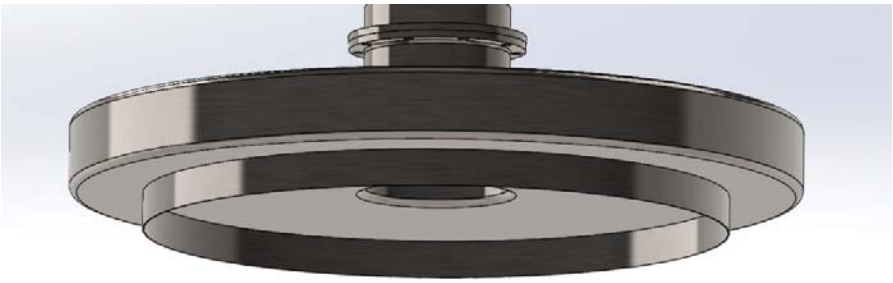

Figure 2-7: Original steel lid

The reactor was designed so that the stack updraft would create a negative pressure, thus any expected leaks would be ingress of air. However, during the peak of gas evolution, the system was found to be at a slight positive pressure, driven by the volatiles evolution. And that the burners are forced draft. The consequence is that fugitive emissions occur, which are a health and safety hazard.

To solve this issue, the bottom panel of the lid and the insulation were removed and replaced with a fire brick material to reduce the effect of expansion and maintain a flat lid. The type of fire cement used for this process was the same as that used to line the combustion chamber of this pyrolyser and therefore is known to be able to withstand very high temperatures of >700°C.

Figure 2-8: Fugitive emissions seen during a pyrolysis run with 70 kg of wood chips

Along with the replacement of the bottom panel with fire cement, a sand pit seal was made in order to ensure any leaking gases would be trapped before they can escape. This was done by welding a trough all the way around the outer perimeter of the top of the reactor and welding a metal ring around the outer rim of the bottom of the lid as shown in figure 2.9. The metal ring will sit inside the sand bed creating a seal which will stop gases from escaping.

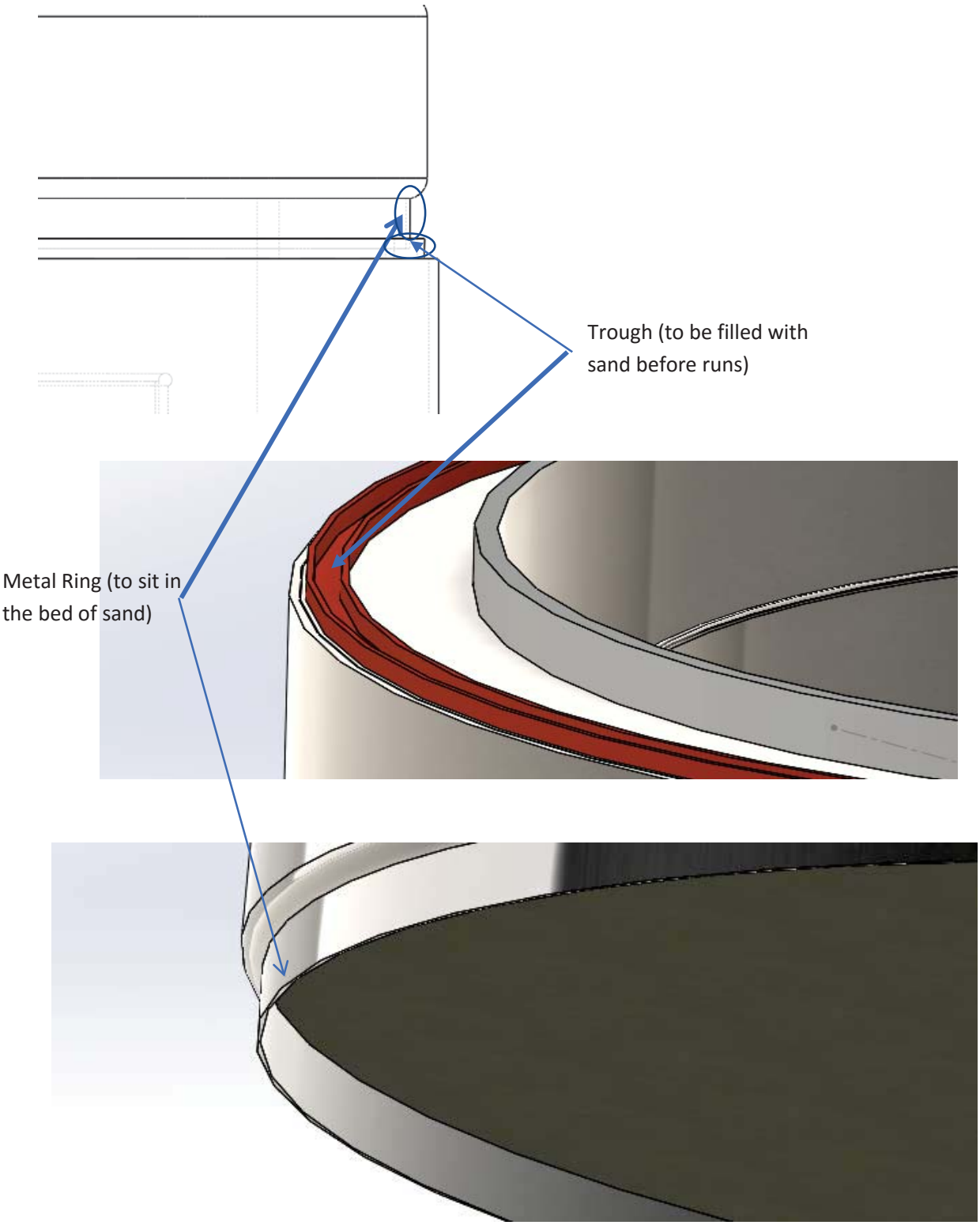

Figure 2-9: Sand seal along the perimeter of the reactor lid

2.3.1. Fire cement

A completely new lid was made instead of modifying the old lid. This had the same dimensions as the old lid with a re-enforced top to hold the extra weight of the cement.

Steel spokes were installed halfway down the lid in order to hold the cement in place once it has been poured and fired.

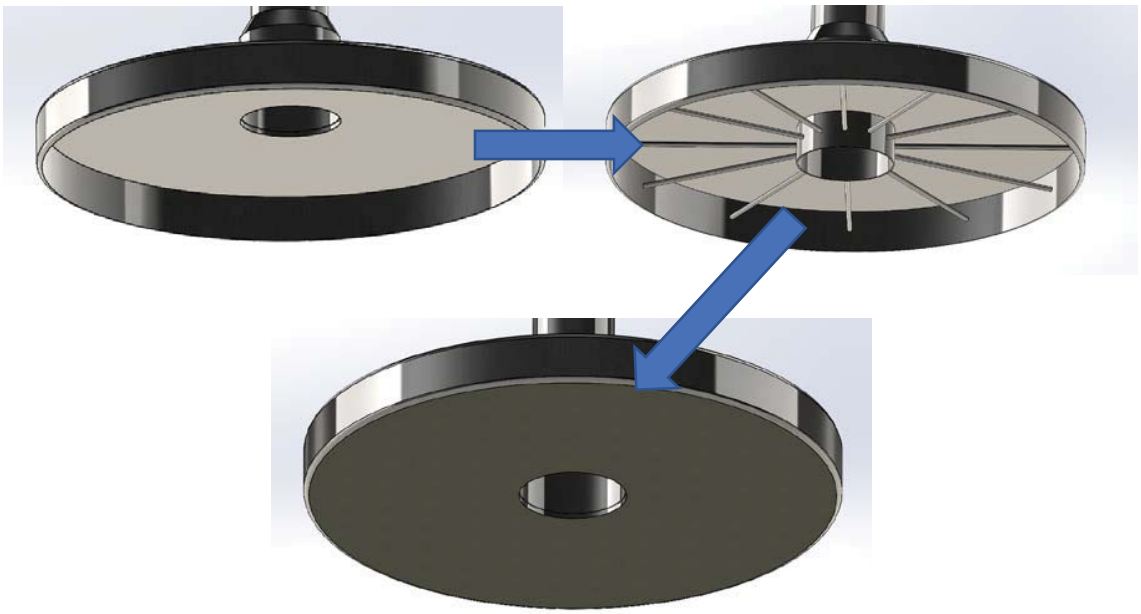

Figure 2-10: 3D representation of the lid modification process. In the top right figure, the bottom sheet metal and insulation are removed. The second imagine on the top-right shows spokes being welded in between the outer flue cylinder and inner wall of the lid. The bottom image shows the completed lid after cement has been poured in.

The spokes were covered in a thin layer of cardboard before pouring the cement; this was then oxidized during the firing process creating a small gap between the steel and cement, allowing the steel spokes to expand independently of the cement during runs, as the materials expand at different rates.

2.3.2. Ventilation holes in combustion chamber

In the combustion chamber, there are 9 ventilation holes which were originally designed to allow excess air to enter the combustion chamber during peak volatile vapour flow. The design of the stack intended the updraft to draw in the air. However, as mentioned in section 2.3, this was found not to occur due to the combined effect of the high evolution rate of volatiles and the forced draft burners. The consequence is that fugitive emissions can also occur from the secondary air vents, which pose a healthy and safety risk. To remove this risk the vents were sealed by filling them with fire cement. It is envisaged that partial combustion can be controlled by the larger 26 kW burner; turning off this burner is a two step process. First gas is turned off with the air flow remaining. This air flow is sufficient for partial or even complete combustion, if desired. However, the current operation takes the safest approach by dumping this air flow external to the combustion chamber. It is not switched off as this would change too much the air flow to the small burner, as they are both supplied by the common blower.

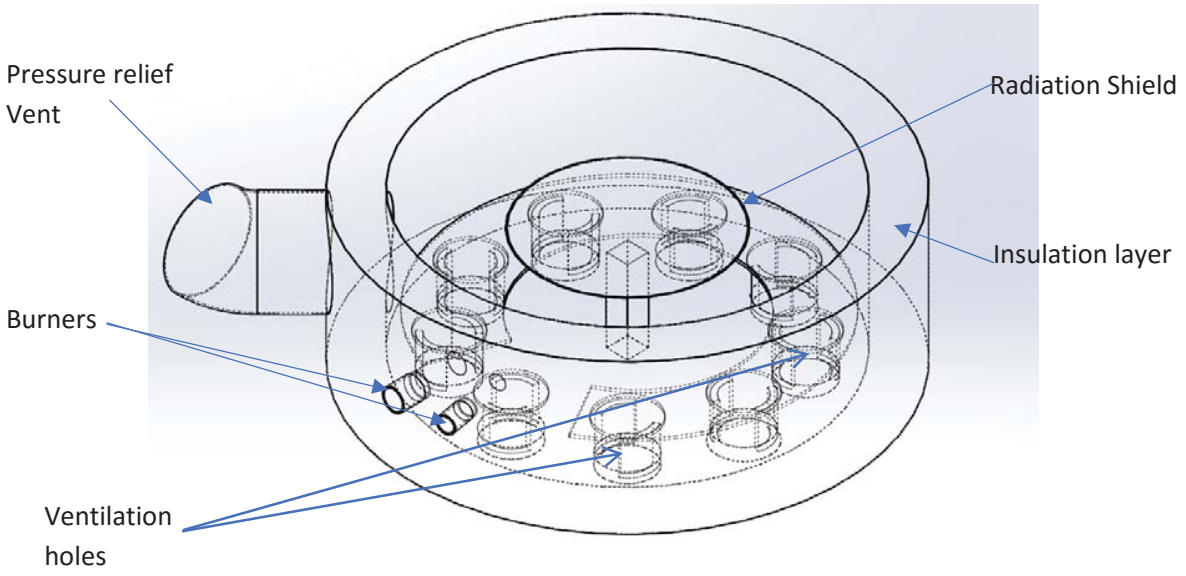

Figure 2-11: Schematic of combustion chamber

2.3.3. Ceramic/synthetic wool insulation

Previously, there was a thin (15mm) ceramic insulating wool rope that sits on the outer rim of the combustion chamber and acts as a seal between the combustion chamber and reactor. This seal was constantly compromised due the mechanical movement of the reactor and chamber as they were heated and cooled, creating leaks. A new wider insulation rope was added which provides a secondary seal.

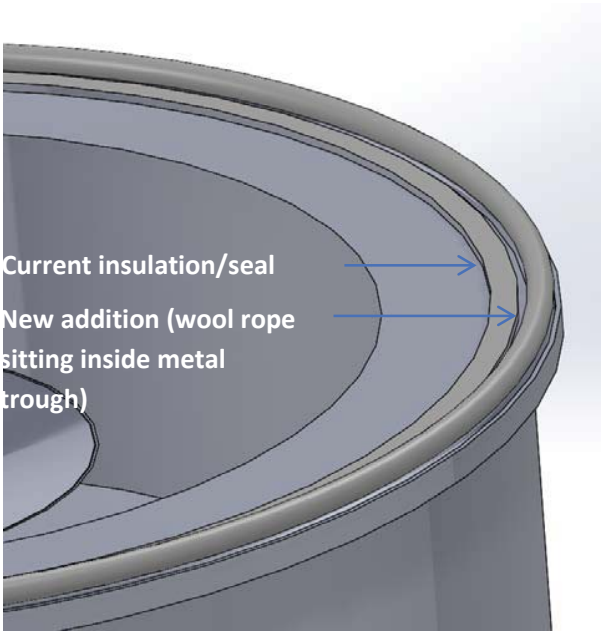

Figure 2-12: New ceramic rope seal around the perimeter of the combustion chamber compared to the old

4. Mathematical description of wood pyrolysis

Wood pyrolysis is a complex problem which involves two separate phases, a solid and a gas phase. The mathematical description of this problem will be discussed in this chapter.

This project was aimed at mathematically modeling the pyrolyser that was designed and built at Massey University by Bridges et al. (Bridges, 2013) Section 3. The model aims to predict:

- Time for completion of the batch cycle
- Pyrolysis product yields including biochar, tar and gas
- Biochar product quality based on a combination of highest treatment temperature and residence time
- Carbon footprint

The mathematical description of this problem will be discussed in this chapter.

Although the production of biochar has been conducted for thousands of years, the heat and mass transfer mechanisms involved are still not well understood. This model aims to simulate the heat and mass transfer occurring in a bed of wood chips (*Pinus radiata)*. Heat is provided externally and is conducted through the steel wall of the reactor and into the wood. Wood is then heated to critical temperatures for water evaporation and then for pyrolysis. The partial pressure created by the formation of vapours then drives the movement of gases through the porous bed, heating it convectively. Radiative heat transfer also becomes increasingly important as the pyrolyser heats up. The expected temperature range is 20°C-700°C.

COMSOL Multi physics was chosen as the program in which to solve this model, because of its multi physics approach to modeling and has a user friendly interface. COMSOL also offers the option to convert the model into an application and allow user access to the model without actually having the program installed. This will be useful in achieving the ultimate goal of this project, which is to produce an open source pyrolyser with a comprehensive model that users

can easily use to predict biochar yields, quality, carbon footprint and time for completion based on their feedstock material parameters.

4.1. Conceptual model

Figure 4.3 below shows a cross-sectional view of the system, which is a cylindrical packed bed reactor of wood chips with a perforated core. It has a combustion chamber at the bottom which provides the heating for the process.

At start up, two burners underneath the pyrolysis drum (figure 4.3) provide a total of 30 kW of heat to initiate the process. Heated gases flow from the combustion chamber up and around an annular zone between the inner reactor and the insulated outer wall of the outer wall. Heat is transferred from the hot gases onto the surface of the reactor wall via radiation and convection. Heat quickly conducts through the thin steel wall (5 mm) and is radiated onto the wood particles closest to the wall (first particles). Heat is also conducted from the steel wall onto particles in direct contact with the steel wall at a rate based on the temperature difference (gradient).

Some radiative heat is scattered onto surrounding particle surfaces and subsequently absorbed and scattered at a rate based on the scattering and absorption coefficients of the wood. Heat is also conducted out of the particles towards cooler regions in the reactor.

Apart from the radiation and conduction in the near wall region, the subsequent heat flow towards the central perforated core is mostly convective, with an increasing radiative component as the system heats up. Convective heat transfer occurs as the gas and volatiles move through the bed. Cycles of condensation and volatilization will occur for those species that are condensable.

For simplicity, it is assumed that once the wood particles reach 100°C, moisture in the form of liquid water (figure 4.1) begins to evaporate (transition from a liquid phase into a vapour phase).

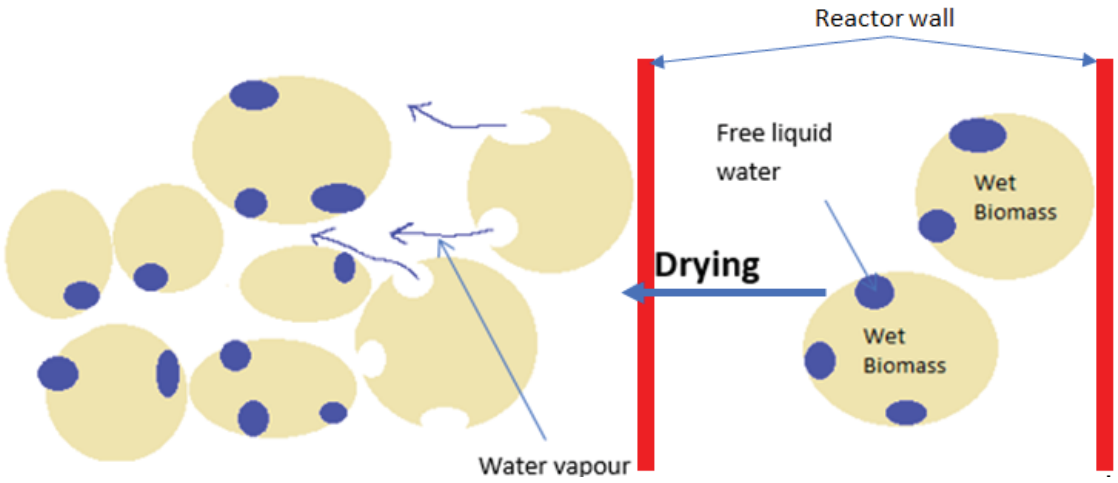

Figure 4-1: Drying of biomass, assuming only free liquid water exists in the wood

When all the moisture from the particle is evaporated, the temperature will begin to rapidly increase again. Only sensible heating occurs between 100 and 200°C. From ~200-280°C, primary pyrolysis reactions, based on Fantozzi et al. (2007) Arrhenius kinetics begin, generating vapour in the form of tars and non-condensable gases and leaving a residue of solid char.

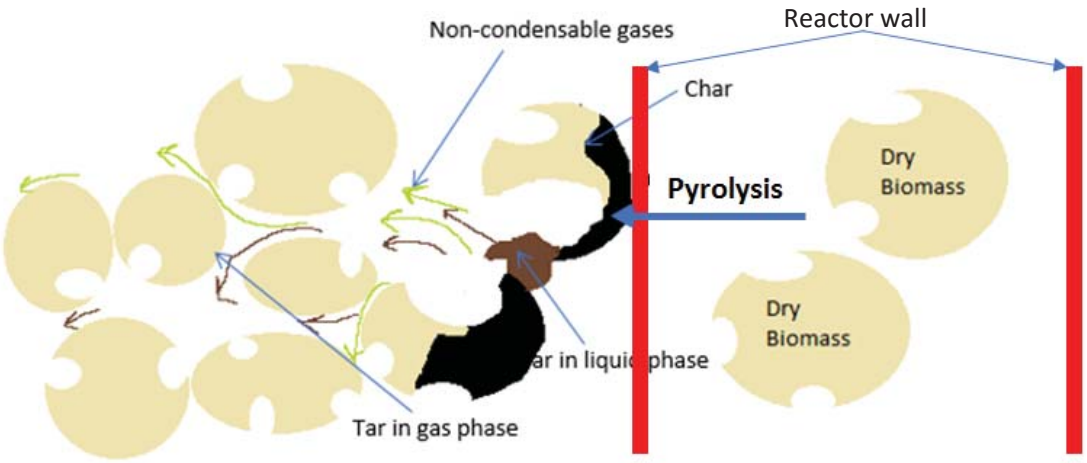

Figure 4-2: Pyrolysis progress as it moves from the wall of the reactor towards the centre (Right to Left)

Water vapour and volatiles will move inward towards the cooler regions of the reactor where they may condense when they come into contact with cool wood surfaces. The condensation process is not modeled in this project. This is unnecessary because the energy of condensation and volatilization is conserved i.e. the two cancel each other out. Mass transport has been modeled by determining a superficial velocity based on Darcy's law (Nield and Bejan, 2013) of fluid flow in porous media. It accounts for the convective heat transfer through the porous bed of wood chips and assumes that the diffusion of vapours through the wood chips (K_p = 1x10^{-13} to 5x10^{-16} m^2 (Blasi, 2000)) is negligible compared to the forced convection through the bed of wood chips, K_a = 2x10^{-5} m^2, estimated from the Carman-Kozeny equation (McCabe, Smith and Harriott, 2005) (4.1), (Calculations can be found in Appendix A) based on their respective permeability, K_i.

$$K = \frac{D_P^2 \varphi_{bed}^3}{180(1-\varphi)^2} \tag{4.1}$$

Where D_P is the average particle diameter (m) and φ_{bed} is the bed porosity (non-dimensional).

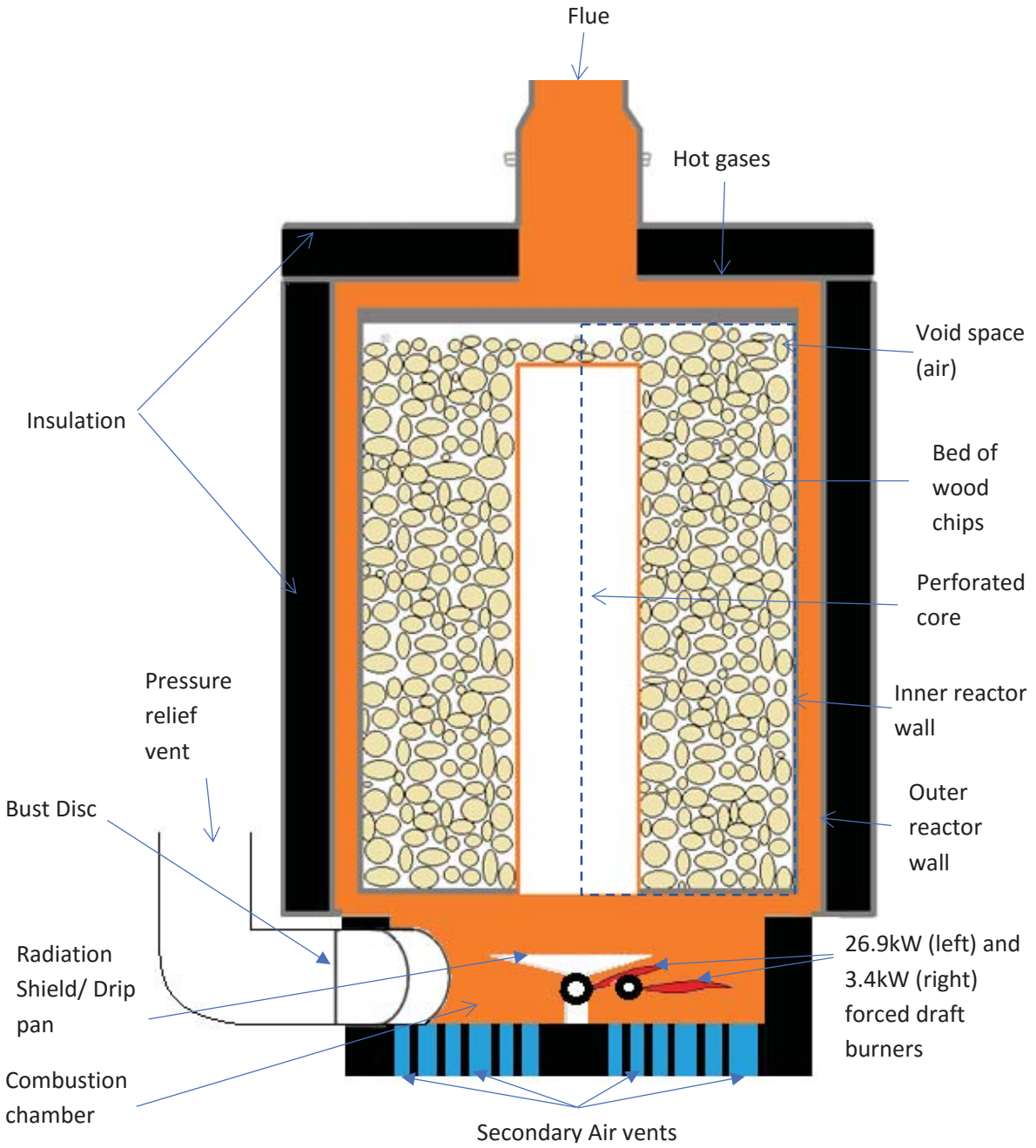

Figure 4-3: Cross-sectional schematic of the pyrolysis reactor. The forced draft burners in the combustion chamber provide heat. The hot gases flow up through the annulus and out the flue. The updraft draws secondary air through the base of the combustion chamber. As heat travels through the pyrolysis chamber walls, the biomass thermally degrades. The volatiles move towards the centre perforated zone through cycles of condensation and re-volatilization. Volatiles then enter the combustion chamber and are partially combusted by ignition from the burners and the secondary air. Partial combustion is ensured by designing the secondary air vents and to limit supply. The dashed line shows the boundary of the model developed in this work.

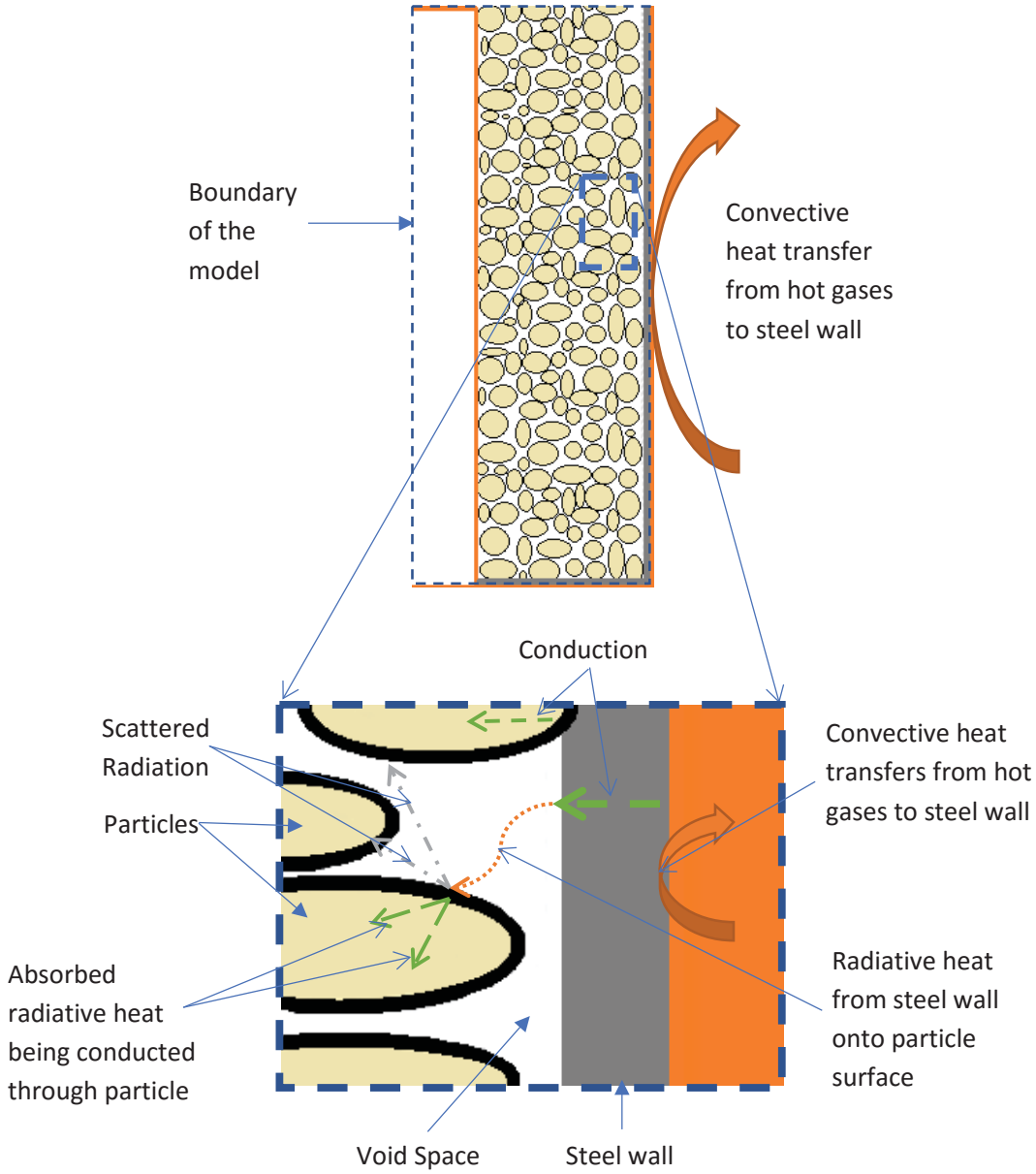

Figure 4-4: Schematic of the heat transfer mechanisms occurring at the walls of the reactor (this does not include convective heat transfer). Here the green dashed arrows represent heat transfer via conduction. Curved dotted arrows in orange represent heat transfer via radiation. Grey dotted-dashed line represent scattering radiation coming off from the wood particles. Once volatiles form, subsequent heat transfer is mostly by convection and radiation.

4.2. Assumptions

The following assumptions are made about the bed of particles within the system shown in figure 4.4:

1. The bed of wood chips is a homogeneous porous reacting media.
2. The burners supply 30 kW of heat, which corresponds to a temperature increase because the reactor heats up. To improve the computational speed of COMSOL, the flue gas flow and heat transport was not modeled. Instead, a time dependent temperature profile was assumed, from which the heat flow was back calculated to check that approximately 30 k W was delivered to the reactor. This temperature profile was obtained from experimental measurements of the flue gas temperature. Then, assuming that the top wall of the reactor is at the flue gas temperature, the side wall is 100°C hotter and the bottom 200°C hotter. This gave a fairly accurate heat flux while ensuring fast computation times.
3. No shrinkage of the wood chips occurs in either the radial or tangential directions.
4. No diffusion occurs through the wood chips (internal particle gradients are neglected), only through the large pores between the wood chips.
5. Heat is transferred onto the outside of the steel wall of the reactor via radiation and convection from the heat source (LPG) gases. However, the resistance of the wall to heat transfer is neglected, due to its high conductivity and the wall being very thin.
6. Reaction kinetics are based on the model proposed by Fantozzi (2007). For this model, both primary and secondary reaction are considered and along with the evaporation of water. They are all modeled with an Arrhenius correlation.
7. The Condensation and re-evaporation cycles were ignored in this model. The reactor transports heat from the outer drum wall to the core by radiation, conduction and through convection by the volatiles and gases. The model observes these forms of transport including the initial water evaporation of water and volatilization of tar volatiles, but thereafter convection mass transport only transfers heat due to sensible

heat change. It does not follow cycles of condensation and re-volatilization. This is not necessary because it does not affect the overall heat balance because components only leave the system as volatiles or gases. Thus, the net heat transferred over a distance is simply the sensible heat change of the water vapour, volatiles or gases. Ignoring the stasis at 100°C for water and various condensation temperatures for fractions of the tar (which indeed, are unknown), will only affect local temperature profiles and not the overall change in system temperature that occurs over many hours.

8. Only water in the lumen (free-liquid water) is considered
9. There is no temperature gradient at the perforated core of the reactor.

The following section describes the pyrolysis kinetics and the conservation equations.

4.3. Pyrolysis kinetics

The following pyrolysis scheme, from section 1 (figure 1.3) and described by Fantozzi (Al., 2007) is presented here for reference with the conservation equations below

Primary Reactions:

$$Wood \xrightarrow{k_1} Char$$

$$Wood \xrightarrow{k_2} Tar$$

$$Wood \xrightarrow{k_3} Gas$$

Secondary Reactions:

$$Tar \xrightarrow{k_4} Char_2$$

$$Tar \xrightarrow{k_5} Gas_2$$

Water Evaporation:

$$Liquid\ Water \xrightarrow{k_6} Water\ Vapour$$

Table 4-1: Constant values used in the model. Here H is the heat of reaction, A is the Arrhenius pre-exponential constant and E is the activation energy (e.g. Solid phase = wood, char and Gas phase = Tar, Gases, water vapour).

Parameter	Value	Ref
H_1=H_2=H_3 (kJ kg^{-1})	-420	(Di Blasi, 1993)
H_4=H_5 (kJ kg^{-1})	40	(Liden, Berruti and Scott, 1988)
H_6 (kJ kg^{-1})	-2,440	(Chan, Kelbon and Krieger, 1985)
A_1 (s^{-1})	1.44 x 10^4	(Thurner and Mann, 1981)
A_2 (s^{-1})	4.13 x 10^6	(Thurner and Mann, 1981)
A_3 (s^{-1})	7.38 x 10^5	(Thurner and Mann, 1981)
A_4 (s^{-1})	4.28 x 10^6	(Liden, Berruti and Scott, 1988)
A_5 (s^{-1})	1.00 x 10^5	(Di Blasi, 1993)
A_6 (s^{-1})	1.53 x 10^{10}	(Chan, Kelbon and Krieger, 1985)
E_1 (kJ mol^{-1})	88.6	(Thurner and Mann, 1981)
E_2 (kJ mol^{-1})	112.7	(Thurner and Mann, 1981)
E_3 (kJ mol^{-1})	106.5	(Thurner and Mann, 1981)
E_4 (kJ mol^{-1})	107.5	(Liden, Berruti and Scott, 1988)
E_5 (kJ mol^{-1})	107.5	(Di Blasi, 1993)
E_6 (kJ mol^{-1})	88.6	(Chan, Kelbon and Krieger, 1985)

The rate constants k_1-k_6 are described using Arrhenius kinetics with the constants shown in table 4.1. The kinetics are of the form

$$k_i = A_i \exp\left(-\frac{E_i}{RT}\right) \tag{4.2}$$

4.3.1. Conservation of mass

The principle of conservation of mass states that for a closed system, the mass of the system does not change over time or for an open system that the flow in plus the accumulation within the system equals the flow out. In this system the pyrolysis reactor contains an initial mass of wood chips, so there is no flow in. Only gases and volatiles are assumed to leave the system.

The overall balance is (after the concentrations have been converted back to actual mass basis kg m^{-3} by multiplying by their molar masses):

$$\frac{\partial C_w}{\partial t} + \frac{\partial C_m}{\partial t} + \frac{\partial C_c}{\partial t} + \frac{\partial C_T}{\partial t} + \frac{\partial C_g}{\partial t} + \frac{\partial C_v}{\partial t} = 0 \qquad (4.3)$$

Concentrations are used because a basis of 1 m^3 of reactor volume is assumed. Therefore C_w represents the bulk density of dry wood chips and C_m represents the bulk density of free water distributed within the volume.

COMSOL multi physics uses molar concentrations rather than mass concentrations. Therefore, conversions are made using the values shown in table 4.1.

In pyrolysis, the rate of thermal conversion of wood (wood consumption) is equal to the rate at which the primary reaction products are being produced.

$$\frac{\partial c_w}{\partial t} = \frac{\partial C_w}{\partial t}\left(\frac{1}{M_w}\right) = -(k_1 + k_2 + k_3)\left(\frac{\rho_w}{M_w}\right)[mol\ m^{-3}s^{-1}] \qquad (4.4)$$

Here, c_w is the concentration of wood, mol m^{-3}, ρ_w is the density of wood, kg m^{-3} and M_w is the molar mass of wood, kg mol^{-1}. The k term describes the rate of reactions, with the subscripts 1-3 accounting for the first three primary reactions. Since wood is being consumed, there is a negative sign at the start of the RHS to represent this.

Char is created in two steps. First, primary char is created from the decomposition of wood at the reaction rate k_3. Secondary char is also created via re-polymerization reactions in the vapour phase from tar that is in contact with char at the rate of k_5.

$$\frac{\partial c_c}{\partial t} = k_3 \left(\frac{\rho_w}{M_w}\right) + k_5 \left(\frac{\rho_T}{M_T}\right) [mol\ m^{-3} s^{-1}] \tag{4.5}$$

Where, ρ_T is the density of tar, kg m^{-3} and M_T is the molar mass of tar, kg mol^{-1}. The molar mass of tar used is the molar mass of benzene, following the work of Grønli (1996).

Tar is first produced through the consumption of wood at the reaction rate k_2 and is then converted into secondary gas and char at the reaction rates k_4 and k_5, respectively.

$$\frac{\partial c_T}{\partial t} = k_2 \left(\frac{\rho_w}{M_w}\right) - (k_4 + k_5) \left(\frac{\rho_T}{M_T}\right) [mol\ m^{-3} s^{-1}] \tag{4.6}$$

Gas is produced via two independent reactions. Primary gas is produced by primary reactions by consuming wood at the reaction rate k_1. Later on in the pyrolysis process, secondary gas is also produced from tar at the reaction rate k_4.

$$\frac{\partial c_g}{\partial t} = k_1\left(\frac{\rho_w}{M_w}\right) + k_4\left(\frac{\rho_T}{M_T}\right)[mol\ m^{-3}s^{-1}] \quad (4.7)$$

For this model, water is modeled using an Arrhenius relationship with the reaction rate k_6 representing the rate at which liquid water in the pores is converted into water vapour. This technique is used in other drying studies (Chan and Krieger, 1983).Therefore, similar mass conservation equations can be applied to the evaporation of water.

$$\frac{\partial c_M}{\partial t} = -k_6\left(\frac{\rho_M}{M_{H_2O}}\right)[mol\ m^{-3}s^{-1}] \quad (4.8)$$

Here, M_{H2O} is the molar mass of water. The mass conservation reaction has a negative on the RHS to represent the consumption of water as it is being converted into water vapour.

$$\frac{\partial c_V}{\partial t} = k_6\left(\frac{\rho_M}{M_{H_2O}}\right)[mol\ m^{-3}s^{-1}] \quad (4.9)$$

Water vapour and volatiles are flowing across the reactor from the hot annulus towards the core. The local concentration of the gas and volatiles therefore depend both on the flux entering the local region plus local generation via thermal degradation, minus the flux leaving.

The mass transport is governed by equation 4.10 below. The first term on the left-hand side (LHS) corresponds to the accumulation (or consumption) of species in a local region. The second term accounts for the diffusion of the species within the solvent and the third term accounts for the transport via convection of the species. The term on the right-hand side (RHS) of the equation, J_i accounts for the production (source) of the species, usually due to a chemical reaction, in this case, this is the production of tar, gas and char and the consumption of wood.

$$\frac{\partial c_i}{\partial t} + \nabla.(-D\nabla c_i) + u.\nabla c_i = J_i \quad (4.10)$$

where,

c_i = Concentration of species i, mol m^{-3}

D = Mass Diffusion Coefficient of species, $m^2\ s^{-1}$

$J_i = \frac{\partial c_i}{\partial t} = k_i c_i$= Reaction rate expression for the consumption or generation of species,

mol $m^{-3}s^{-1}$

u = the velocity vector, m s^{-1}

This mass transport is further complicated by the discrete nature of the system. Generation only occurs within particles and transport (except volatiles diffusing from particles) only occurs in the interstices between particles. As the system is a pyrolysis reactor containing 10^4-10^5 wood chips, any local region will contain many particles. At the system (rather than particle) scale of scrutiny the problem can be treated as a porous media which is able to be modeled in COMSOL multi physics by selected the porous media sub model. Mass transport through this porous media is driven by the pressure gradient for convection and the individual species vapour pressure gradient for convection and the individual species vapour pressure gradient for diffusion. For the latter, an effective diffusion coefficient D_e is used. D_e is highly dependent on the porous media structure and gas/liquid phases travelling within. For this model, the flow is assumed to be a partially saturated bed of wood with volatilization, and thus the following relationship was used:

$$D_e = \frac{\epsilon}{\tau_L} D_L + \frac{a_v}{\tau_G} v_G D_G \quad (4.11)$$

Where,

$\tau_{L,G}$= tortuosity of the bed for the movement of liquid and gas phases through the bed, (-)

$D_{L,G}$ = Diffusion coefficients for species in the liquid and gas phases, $m^2\ s^{-1}$

$v_G = \frac{\partial_{ci}}{\partial_t}$ =rate of volatilization of species i, mol $m^{-3}\ s^{-1}$

a_v = gas volume fraction, (-)

However, due to the discussion above the pressure driven forced convection is dominant. The effective porous media diffusion coefficient will have minimal impact. In fact, it proved to be negligible.

4.3.2. Conservation of momentum

The challenge then to establishing the local concentration is to understand the convective motion of the gases and volatiles across the bed. This is captured by the momentum equation because pressure is the driving force. Pressure increases where thermal decomposition generates gases. It then forces these gases through the resisting porous bed towards the central core of the reactor. However, pressure does not always need to be considered. In open porous systems where the overall pressure gradient is low, the gases once formed can be assumed to move towards the region of low pressure, i.e., the central perforated core of this reactor. The system studied here is a combination. Individual particles are porous but with considerable internal resistance to mass transfer. The interstices between the particles however, are open with low resistance. In developing the model here the bed is simply assumed porous without any 'scale of scrutiny' discrimination. Therefore, this model includes the calculation of a pressure gradient to drive the heat and mass transfer. In this way, the model is rigorous in that it includes the conservation of momentum.

Here pressure is considered. Darcy's Law shows that the velocity of the volatile species is proportional to the internal pressure gradient and the material's permeability divided by the

gas viscosity. The generalized momentum balance in porous mediums can be written in terms of the Darcy equation (4.12).

$$-\nabla P = \frac{\mu u}{K} \tag{4.12}$$

where,

K = permeability, m^2

μ =dynamic viscosity of the fluid, Pa s

∇P = the pressure gradient within the porous matrix, Pa

Permeability changes as pyrolysis progresses; η ($0 \leq \eta \geq 1$ is the extent of conversion of wood to char).

For this case of a wood chip packed bed reactor, this form of the Darcy equation is not suitable as it does not allow for the ability to assign no-slip conditions at the boundary surface. For highly porous media (φ = 65%) with no-slip boundary conditions, the Brinkman equation (4.13) is often used, which is an extension of Darcy's law.

$$\rho\left[\frac{\partial u}{\partial t} + \nabla \cdot (u^2)\right] = -\nabla p + \mu\nabla^2 u \tag{4.13}$$

When the above equation (4.13) is integrated with respect to a volume and with the aid of equation (A3.2, Appendix C) gives (Hsu and Cheng, 1990):

$$\underbrace{\rho\left[\underbrace{\frac{\partial}{\partial t}(\varphi\bar{u})}_{\text{Unsteady acceleration}} + \underbrace{\overline{\nabla}\cdot(\varphi\bar{u}^2)}_{\text{Convective acceleration}}\right]}_{\text{Inertia}} = \underbrace{-\overline{\nabla}(\varphi\bar{p})}_{\text{Pressure gradient}} + \underbrace{\mu\overline{\nabla}^2(\varphi\bar{u})}_{\text{Viscosity}} + \underbrace{B + F}_{\text{Other forces}} \tag{4.14}$$

Divergence of stresses

where, the term B is the total volumetric drag force (Appendix C shows the derivation of this force) and F is the volumetric body force of the transporting fluid which, in most cases only the force due to gravity is significant enough to be considered. The term u can be dissected into the sum of the intrinsic phase average velocity, $\bar{u}$ and the deviation velocity, u'.

$$u = \bar{u} + u' \tag{4.15}$$

Substituting equation 4.15 into 4.14 gives:

$$\rho_f \left[\frac{\partial}{\partial t}(\varphi\bar{u}) + \overline{\nabla} \cdot (\varphi\bar{u}^2) + \overline{\nabla}(\varphi u'^2)\right] = -\overline{\nabla}(\varphi\bar{p}) + \mu\overline{\nabla}^2(\varphi\bar{u}) + B + F \tag{4.16}$$

The microscopic inertial term (second on left hand side) is usually not important when compared to the terms on the right hand side, where the pressure gradient is balanced by the body force (due to gravity), except near a wall boundary where Brinkman's frictional effect predominates. The third term on the LHS is of higher order than the second term and therefore can be neglected. Equation 4.16 can therefore be simplified:

$$\rho\left[\frac{\partial u}{\partial t} + \overline{\nabla} \cdot \left(\frac{u^2}{\varphi}\right)\right] = -\overline{\nabla}p + \mu\nabla^2 u + B + F \tag{4.17}$$

Equation 4.17 is the general convective form of the Brinkman equation for porous media as given by Hsu et al. (1990).

For a Newtonian compressible fluid equation 4.17 becomes 4.18 for the case of a gas movement along a conduit driven by a pressure gradient without considering porosity, such as the pyrolysis gases in this example, the following equation is used (notice $\mu\nabla^2 u$ becomes the second and third term on the RHS of eq. 4.18):

$$\rho\left(\frac{\partial u}{\partial t} + u \cdot \nabla u\right) = -\nabla p + \nabla \cdot (\mu(\nabla u + (\nabla u)^T) + B + F \tag{4.18}$$

When plugging in the drag force B from Appendix C, and $F = \rho g$, then equation 4.18 can be presented as equation 4.19:

$$\rho\left(\frac{\partial u}{\partial t}+\overline{\nabla}\cdot\left(\frac{u^2}{\varphi}\right)\right)=-\overline{\nabla}p+\nabla\cdot(\mu(\nabla u+(\nabla u)^T)-\left[\frac{\mu\varphi u}{K}+\rho\frac{F\varphi u|u|}{\sqrt{K}}\right]+\rho g \quad (4.18)$$

Equation 4.18 can be written as follows to include a mass source or sink over a porous media domain:

$$\frac{1}{\varphi_{bed}}\rho\frac{\partial u}{\partial t}+\frac{1}{\varphi_{bed}}\rho(u\cdot\nabla)u\frac{1}{\varphi_{bed}} = \nabla\cdot\left[-pI+\mu\frac{1}{\varphi_{bed}}(\nabla u+(\nabla u)^T)\right]-\left(\frac{\mu}{K}+\beta_F|u|+\frac{Q_{br}}{\varphi_{bed}^2}\right)u + F \quad (4.19)$$

where,

β_F = Forchheimer's drag force, kg m^{-4}

I = Identity matrix[3]

Q_{br}= Mass source or sink, kg m^{-3}

Because of the variable density of the fluid as pyrolysis progresses, the two equations are solved with the ideal gas law (volatiles are assumed to behave like a perfect gas).

$$\frac{\partial}{\partial t}(\varphi_{bed}\rho)+\nabla\cdot(\rho u)=0 \quad (4.20)$$

And the continuity equation becomes:

$$\rho\nabla\cdot u=Q_{br}$$

and density of the mixture can be determined by

$$p=\frac{\rho_g RT}{M_g} \quad (4.21)$$

[3] In linear transformation where it converts every tensor into itself is called an identity tensor, denoted by the symbol I. For example: Ia = a for any vector a.

where,

ρ_g= Density of the gas, kg m^{-3}

M_g= Average molar mass of the vapour, kg mol^{-1}

R = Ideal gas constant, 8.314 J mol^{-1} K^{-1}

T = Temperature of gas, K

The final term on the RHS is F which is the resultant gravitational force on the fluid in the porous matrix and is accounted for by the following equation. This force is minimal and can be ignored but was added in this model because it did not negatively influence computational time.

$$\boldsymbol{F} = Volume\ force\ due\ to\ gravity = \rho g_{constant} \tag{4.22}$$

where $g_{constant}$is the acceleration due to gravity, -9.81 m s^{-2}.

The effective permeability K_{eff} is determined by the mixture rate from those of wood and char.

$$K_{eff} = \eta K_w + (1-\eta)K_c \tag{4.23}$$

where, K_w is the permeability of wood and K_c is the permeability of char, and η the pyrolysis reaction progress variable, $0 \leq \eta \geq 1$:

$$\eta = \frac{m_w}{m_{w,i}} \tag{4.24}$$

Where, m_w is the current mass of unreacted wood and $m_{w,i,}$ is the initial mass of unreacted wood.

4.3.3. Conservation of energy

Heat is conserved in the same way the mass and momentum are conserved. Heat is transferred into the bed of wood via conduction, radiation and convection. The following describes heat transfer across the boundary of the problem shown in figure 4.1.

This overall balance equation divides the heat entering into parts; that which is needed to evaporate moisture, that which is needed to drive endothermic reactions, that which is generated by exothermic reactions.

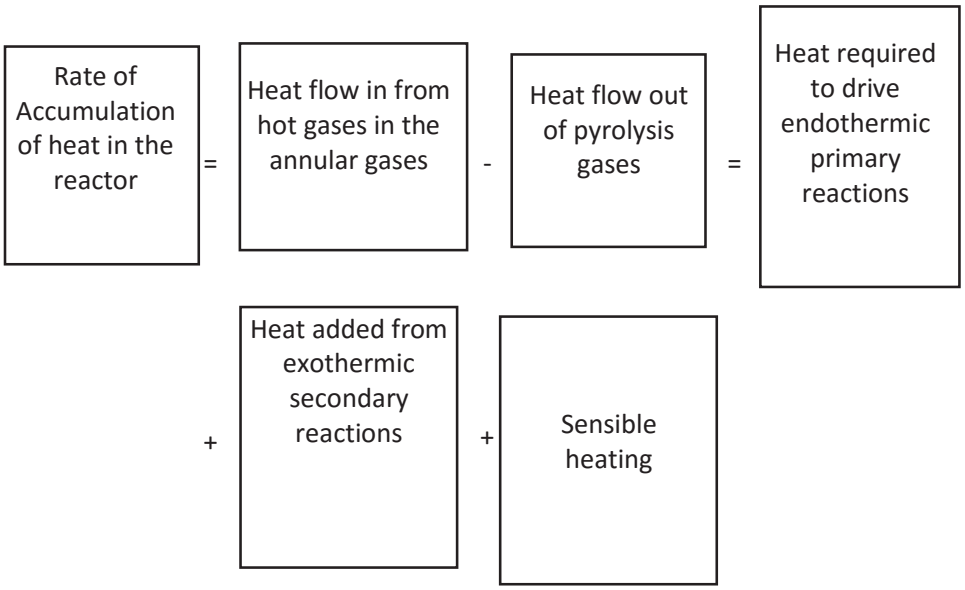

Within the reactor boundary, heat flows from the flue gas annulus to the reactor wall, through the wall, then into the nearby particles. Thereafter heat flows mostly by convection as hot gases and volatiles travel through the bed. The first transfer from the flue gas annulus to the reactor wall, occurs by radiation and convection. The second, through the wall occurs by

conduction. However, a simpler approach was used to save computational effort as discussed in section 4.2. By defining the wall temperatures over time matched with experimental data, the external heat flux of ~30 kW was obtained. The third into the woody particles occurs by radiation and conduction. The fourth is as above. Each is discussed below.

4.3.3.1. Heat flow from the gas annulus to the reactor wall

While the simplification of assuming wall temperature made the computation quicker, the problem was at first set up as heat transfer from a hot gas. The heat flux, provided by the hot gases transferring heat to the outside of the reactor walls is calculated using the following standard heat transfer equation:

$$q_{conv} = h(T_{ext} - T) \tag{4.25}$$

where, q is the heat flux (W m^{-2}), h is the convective heat transfer coefficient (W m^{-2} K^{-1}) and T_{ext} is the external temperature (K). The reactor is considered as a long cylinder with a Reynold's number of 2.7 x 10^3 and a Rayleigh number of 3.2 x 10^3 calculated (Appendix B) for the flow of gases in the annular zone (jacket) of the reactor. The following two correlations (Equations 4.26 and 4.27) can be used to approximate the heat transfer coefficient (Incropera *et al.*, 2006). For this model, equation 4.27 was selected.

$$h = 2\frac{\kappa}{L}\mathrm{Pr}^{\frac{1}{3}}\left(0.037Re_L^{\frac{4}{5}} - 871\right) \; if \; Re_L > 5 \times 10^5 \tag{4.26}$$

$$h = \frac{\kappa}{L}\left(0.68 + \frac{0.67 Ra_L^{\frac{1}{4}}}{\left(1 + \left(\frac{0.492\kappa}{\mu C_P}\right)^{\frac{9}{16}}\right)^{\frac{4}{9}}}\right)^2 \quad if\ Ra_L \leq 10^9 \qquad (4.27)$$

where,

Re_L = Reynold's Number, $\rho UL/\mu$

Ra_L= Rayleigh number, $\rho^2 g \Omega_p C_p \Delta T L^3/\mu k$

Pr = Prandtl number, $\mu C_p/k$

ρ = fluid density, kg m^{-3}

L = characteristic length (volume of the cylinder divided by the surface area), m

ΔT = temperature difference between the surface and hot gases (T_{ext}-T), K

g = acceleration due to gravity, m s^{-2}

κ = thermal conductivity of the hot gases, W m^{-1} K^{-1}

μ = dynamic viscosity of the hot gases, Pa.s

C_p = heat capacity of the hot gases, J kg^{-1} K^{-1}

Ω_p = coefficient of thermal expansion, K^{-1}

D = diameter of the cylinder, m

U = averaged velocity, m s^{-1}

A typical value for the heat transfer co-efficient was calculated from equation 4.27 (Appendix B) as:

$$h = \frac{61.8 \times 10^{-3}}{0.136}\left(0.68 + \frac{0.67(3.2 \times 10^{3})^{\frac{1}{4}}}{\left(1 + \left(\frac{0.492(61.8 \times 10^{-3})}{(37.44 \times 10^{-6})(1.196)}\right)^{\frac{9}{16}}\right)^{\frac{4}{9}}}\right)^{2}$$

$$h = 1.25\ W\ m^{-2}K^{-1}$$

4.3.3.2. Heat transfer through the reactor wall

Heat transfer is by conduction, defined by

$$q = -\kappa(T_o - T_{in}) \tag{4.28}$$

where κ is the thermal conductivity of the solid material, (W m^{-1} K^{-1})and $T_o - T_{in}$ is the difference between the outside (o) and inside (in) wall temperatures, K.

Because the wall is thin and steel is highly conductive, this effectively means the resistance to heat transfer in the steel wall is very low. Indeed, it was computationally easier to remove the wall without affecting the results.

4.3.3.3. Heat transfer from reactor wall to nearby particles

The hot wall radiates heat into nearby particles and conducts heat into particles that are in contact with the steel wall. Heat flows out of the near-wall boundary by convection and radiation. Conduction is small and can be neglected.

Accumulation of heat in the particles near the inner reactor wall	=	Heat flow into the wood chips by radiation and conduction	-	Heat flow out of the wood chips by radiation, convection and conduction	-	Heat consumed to evaporate water	-	heat out with the flow of water vapour by convection

The heat flow in wall of the reactor is defined by an effective thermal conductivity that includes radiation, κ_{bed}. This is discussed in section 4.3.3.4. The flow out of the boundary wall is that carried by the evolved water vapour, volatiles and gases.

$$Heat\ out\ of\ the\ boundary\ region = (\rho_w h_w + \rho_T h_T + \rho_g h_g)UA \quad (4.29)$$

Where the subscript w is water vapour, T is pyrolysis volatiles (tars) and g is pyrolysis gases. The accumulation term is the sensible heat gain of the remaining solid phase. The gas phase accumulation will be negligible because of the relatively small densities of the gas to solid, and so can be ignored.

4.3.3.4. Heat transfer across the bed of wood chips

By assuming heat flux, q over the height of the pyrolyser wall, only radial heat transfer need be considered. If the heat flux is also equal, then angle is not important either. Nevertheless, COMSOL Multi-physics 5.2 allows the entire 3D problem to be investigated. However, axi-symmetry can be assumed and so the problem of heat transfer across a region within a bed of wood chips reduces to radial and axial co-ordinates. Thus the heat flux into or out of a region can be represented by heat conduction between contacting solid, convection by hot gases and radiation from between particle surfaces (Refer to figure 4.4.). Accumulation is determined by

sensible heat change. Generation is negative for water evaporation and primary reactions and positive for secondary reactions.

The heat transfer across the porous bed of wood, is governed by:

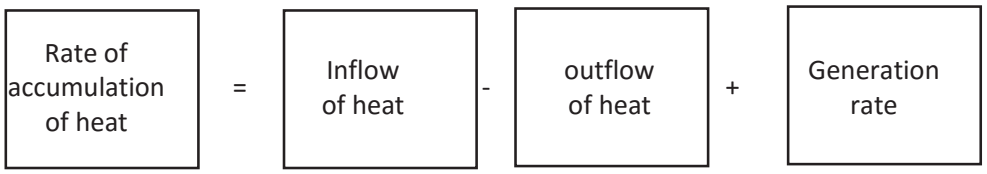

$$(\rho C_P)_{eff}\frac{\partial T}{\partial t} + \rho C_P u.\left[\frac{1}{r}\frac{\partial}{\partial r}\left(\frac{\partial T}{\partial r}\right)\right] + \left[\frac{1}{r}\frac{\partial}{\partial r}\left(-kr\frac{\partial T}{\partial r}\right)\right] + Q = 0 \qquad (4.30)$$

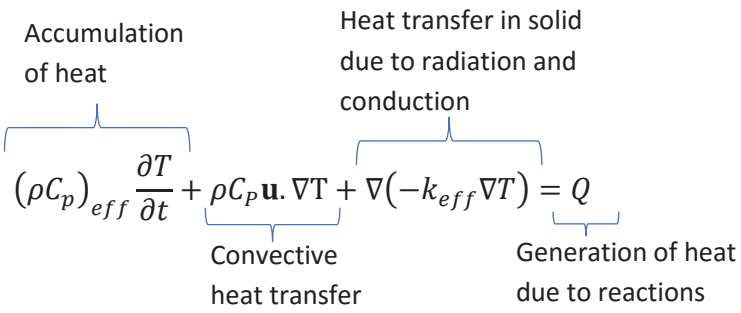

where,

ρ = density, kg m^{-3}

C_P = Heat capacity, kJ kg^{-1} K^{-1}

T = Absolute temperature, K

κ = Thermal conductivity, W m^{-1} K^{-1}

Q = Heat source (or sink) = $\Delta H_i\ R_i$, W m^{-3}

ΔH_i= Enthalpy of reactions for species i, kJ mol^{-1}

R_i = Reaction rate of species i, kg m^{-3} s^{-1}

Where $(C_P)_{eff}$ is the effective heat capacity at constant pressure, (J kg^{-1} K^{-1}), κ_{eff} is the effective thermal conductivity, (W m^{-1} K^{-1}) which is discussed later in section 4.6 and u is the velocity of the fluid, (m s^{-1}) which is calculated using Brinkman equation of fluid flow in a porous media (4.14) and is discussed in the conservation of momentum section 4.3.2.

The heat source balance was calculated by summing the energy absorbed by the primary endothermic chemical pyrolysis reactions and evaporation of moisture and the energy produced by the secondary exothermic reactions.

Primary reactions

Secondary reactions

$$Q = -c_w k_1 \Delta H_c - c_w k_2 \Delta H_T - c_w k_3 \Delta H_g - c_M k_6 \Delta H_6 - c_T k_4 \Delta H_{g2} - C_T k_5 \Delta H_{c2}$$

Evaporation

4.6. Material properties

A large number of material properties have been used in this simulation. Properties of the feedstock material (*Pinus radiata*) were not experimentally collected, but properties were retrieved from literature to closely match those of the feedstock.

Some physical properties such as density and thermal conductivity can vary by up to a factor of 2 between species, while the ability of the wood to allow fluid to pass through it (permeability) can vary by up to a factor of 100. This model was produced in order to be applicable to any species of wood, as long as the material properties of that particular species are known. The following section highlights the material properties used in this simulation.

Table 4-2: Material properties used in this model

Symbols	Expression	Units	Reference
$C_{P,wood}$	$-9.2 \times 10^{-2} + 4.4 \times 10^{-3}T$	kJ kg^{-1} K^{-1}	(Koch, 1968)
$C_{P,char}$	$0.42 + (2.09 \times 10^{-3})T + (6.85 \times 10^{-3})T^2$	kJ kg^{-1} K^{-1}	(Raznjevic, 1975)
$C_{p,volatiles}$	$-0.10 + (4.40 \times 10^{-3})T - (1.57 \times 10^{-6})T^2$	kJ kg^{-1} K^{-1}	(Raznjevic, 1975)
κ_{wood}	0.35	W m^{-1} K^{-1}	(Grønli, 1996)
κ_{char}	0.1	W m^{-1} K^{-1}	(Grønli, 1996)
$\kappa_{volatiles}$	$7 \times 10^{-5}T + 0.0245$	W m^{-1} K^{-1}	Based on air properties
$d_{pore,wood}$	$5.0 \times 10^{-5}\sqrt{\varphi_p}$	m	(Janssens and Douglas, 2004)
ε_{wood}	0.7	(-)	(Corbetta *et al.*, 2014)
ε_{char}	0.92	(-)	(Corbetta *et al.*, 2014)
K	2.5×10^{-6}	m^2	Appendix A
$\mu_{volatiles}$	$(-3.73 \times 10^{-7}) + (2.62 \times 10^{-8})T$	kg m s^{-1}	(Raznjevic, 1975)
M_{water}	18	g mol^{-1}	-
M_{tar}	110	g mol^{-1}	(Grønli, 1996)
M_{gas}	36	g mol^{-1}	(Grønli, 1996)
P_{atm}	1.01325×10^5	N m^{-2}/Pa	-
$T_{initial}$	20	°C	-
σ	5.6703×10^{-8}	W m^{-2} K^{-4}	-

The significant physical properties of permeability, thermal conductivity and specific heat capacity are discussed below.

Permeability

Permeability is the most important physical property when convective flows are high, such as in this system. It is determined as a function of void volume, particle size and geometry for a fixed bed of particles using the Carmen-Kozeny equation (McCabe, Smith and Harriott, 2005). Calculations are given in Appendix A.

Thermal conductivity

Thermal conductivity of wood is also an important thermo-physical property for establishing the heat transfer rate. For this project, the thermal conductivity of the wood (*pinus* radiata) was not measured. Rather the relationship of Yagi and Kunii (1957) for a packed bed of spherical particles was used to define an effective thermal conductivity of the bed of wood chips (Eq. 4.31). Their relationship accounts for both conduction and radiation as follows (Yagi and Kunii, 1957):

$$\frac{\kappa_{bed}}{\kappa_g} = \frac{\beta(1-\varphi_{bed})}{\gamma\left(\frac{\kappa_g}{\kappa_{s,eff}}\right) + \frac{1}{\left(\frac{1}{\emptyset}\right) + \left(\frac{D_P \kappa_{rs}}{\kappa_g}\right)}} + \varphi_{bed}\beta\left(\frac{D_P \kappa_{rv}}{\kappa_g}\right) \tag{4.31}$$

where, $\kappa_{bed}$is the effective thermal conductivity in a packed bed (W m^{-1} K^{-1}). The term β is defined as the ratio of the average length between the centres of two neighbouring particles, l_v in the direction of heat flow to the average diameter of packing, D_P and usually the value of $\frac{1}{3} + \left(1+\sqrt{3}\right) \times \frac{2}{3}$ is used for randomly packed spherical particles (Yagi and Kunii, 1957).

$$\beta = \frac{l_v}{D_P} \tag{4.32}$$

The term φ_{bed} in equation 4.31 is the porosity of the packed bed. The terms; $\kappa_g$is the thermal conductivity of the gases filling the void space within the particles. The thermal conductivity of air was assumed for this value. Figure 4.5 shows the heat transfer mechanism in a series. The In the cross sectional area C-C' thermal conduction occurs in the solid particles following 1-ϵ, where ϵ is the void fraction. The radiant heat then flows from void to void through the void fraction, ϵ. The influence of thermal radiation can be accounted for by the following terms $\kappa_{rs}$and κ_{rv} , which describe the solid surface-to-solid surface radiation (Equation 4.33) and void-to-void radiation (Equation 4.34), respectively.

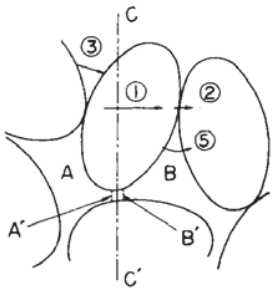

Figure 4-5: The geometry of heat transfer in a particle without flowing fluids. A' and B' are black body surfaces and A and B represent the void space in between. C-C' is the perpendicular direction to heat flow.

$$\kappa_{rs} = 0.1952\left(\frac{\varepsilon}{1-\varepsilon}\right)\left(\frac{T}{100}\right)^3 \tag{4.33}$$

$$\kappa_{rv} = \left(\frac{0.1952}{1+\frac{\varepsilon}{2(1-\varepsilon)}}\right)\left(\frac{T}{100}\right)^3 \tag{4.34}$$

where ε is the emissivity of the bed.

The term $\kappa_{s,eff}$ describes the effective thermal conductivity of the wood. It includes three terms, the maximum thermal conductivity of the void region of the particle (κ_{max}), the minimum thermal conductivity in the solid region (κ_{min}), and the thermal conductivity due to radiation ($\kappa_{s,rad}$).

$$\kappa_{s,eff} = \varphi_P \kappa_{max} + \left(1-\varphi_p\right)\kappa_{min} + \kappa_{s,rad} \tag{4.35}$$

$$\kappa_{min} = \frac{\kappa_g \kappa_{fiber}}{(\varphi_P \kappa_{fiber} + (1-\varphi_P)\kappa_g} \tag{4.36}$$

$$\kappa_{max} = \varphi_P \kappa_g + (1-\varphi_P)\kappa_{fiber} \tag{4.37}$$

Where $\kappa_{fiber}$is the thermal conductivity of wood fiber, (W m^{-1} K^{-1}). φ_P is the particle porosity (non-dimensional). The term $\kappa_{s,rad}$ describes the thermal conductivity due to radiative heat transfer where d_{cavity} is the pore diameter of the particles, m.

$$k_{s,rad} = \frac{4\varphi_p \sigma T_s^3 d_{cavity}}{1 - \varphi_p} \tag{4.38}$$

Specific heat

Another important property to consider when investigating pyrolysis of wood is the wood's specific heat, C_P. which depends on the progress of the conversion of wood to char, where the term η describes the pyrolysis progress (fraction of current virgin wood). The Pyrolysis progress term, η is initially 1, it is calculated in section 4.3.2.

$$C_{P_{eff}} = \eta C_{P_{wood}} + (1 - \eta) C_{P_{char}} \tag{4.39}$$

The specific heat of wood increases with temperature, however for simplicity a constant specific heat capacity of 1500 + T[K] J kg^{-1} K^{-1} (J Ratte *et al.*, 2009) was used for this model. Increase in moisture content also increases the specific heat of wood as extra energy is required to break the wood-water bond. However, this effect is also ignored in this model. The specific heat of char was obtained by Gupta et al. (2003) using differential scanning calorimetry (DSC) and the following relationship was derived

$$C_{P_{char}} = -0.0038T^2 + 5.98T - 795.2 \tag{4.40}$$

where the term T is the temperature in Kelvin.

Similarly, the density of the solid phase is calculated using the following equation

$$\rho_{eff} = \eta\rho_{wood} + (1 - \eta)\rho_{char} \tag{4.41}$$

4.7. Summary

This chapter described the pyrolysis kinetics, governing equations of momentum, heat and mass transfer and the most significant thermo-physical properties for mass and heat transfer within a packed bed of loosely packed particles. The next chapter will address the model implementation in COMSOL.

5. Model implementation in COMSOL Multi-Physics

The pilot scale reactor is a cylinder with the height of 1000 mm and a radius of 375 mm. It has a perforated core in the middle with a height of 900 mm and a radius of 50 mm.

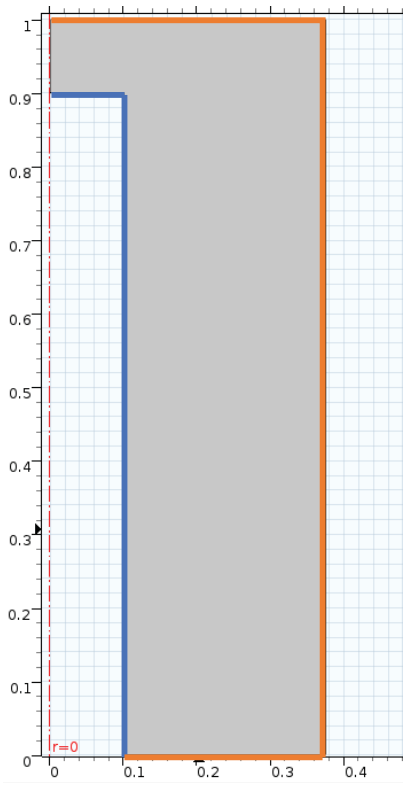

Figure 5-1: Geometry of the model derived from the pilot scale reactor geometry. The blue lines represent the outflow of the heat and mass boundary conditions and the orange lines represent the inward heat source. The grey area is where the porous media was assigned to and all the governing equations of heat, mass and momentum and the reaction kinetics.

Meshing is an iterative process usually determined through trial and error as the user progressively becomes more aware of the dynamics of the physics being modeled. Thus a user must know the results of their model in order to properly mesh the geometry.

In COMSOL Multi physics there are four types of elements that can be used to mesh any 3D geometry. These are:

1) Tetrahedral
2) Bricks (Cubes)
3) Prisms
4) Pyramids

For 2D structures, these four types can be modified and thus triangular and quadrilateral elements are available. This model uses triangular elements suitable for 2D axisymmetric modeling.

Since this is model is dynamic and the rate of change of pyrolysis reactions differs with time, it makes it hard to determine a mesh. The following were considered when deciding what mesh to use for this model.

- Where do the dependent variables (T, u, P_A etc.) change fastest?
- How realistic are the starting (initial) conditions? Must the boundary mesh be refined in order to properly converge to a starting point?
- How much time should be spent solving the model vs. accuracy of the results?

Nevertheless, it still took some time to obtain a solution.

No data was available from experimental runs for the temperature, velocity or pressure within the reactor at the boundary conditions or anywhere else in the bed of wood, thus it was only through trial and error that the rate of the dependent variable changes was determined. It was shown that the solution struggled to come to a starting point, this was due to the assumption that the gases were heated to 1150[K] instantly outside the reactor. Thus, the temperature difference between the outside and inside of the reactor was too great to converge to a reasonable starting point. This took a lot of time to resolve, after which the model was solved much faster with larger time steps. In order to improve the convergence, the boundary mesh was refined to as small an element as possible (figure 5.2) while still being coarse enough to give a reasonable solution time and a ramping temperature profile was used for the boundary heat source instead of an isothermal temperature.

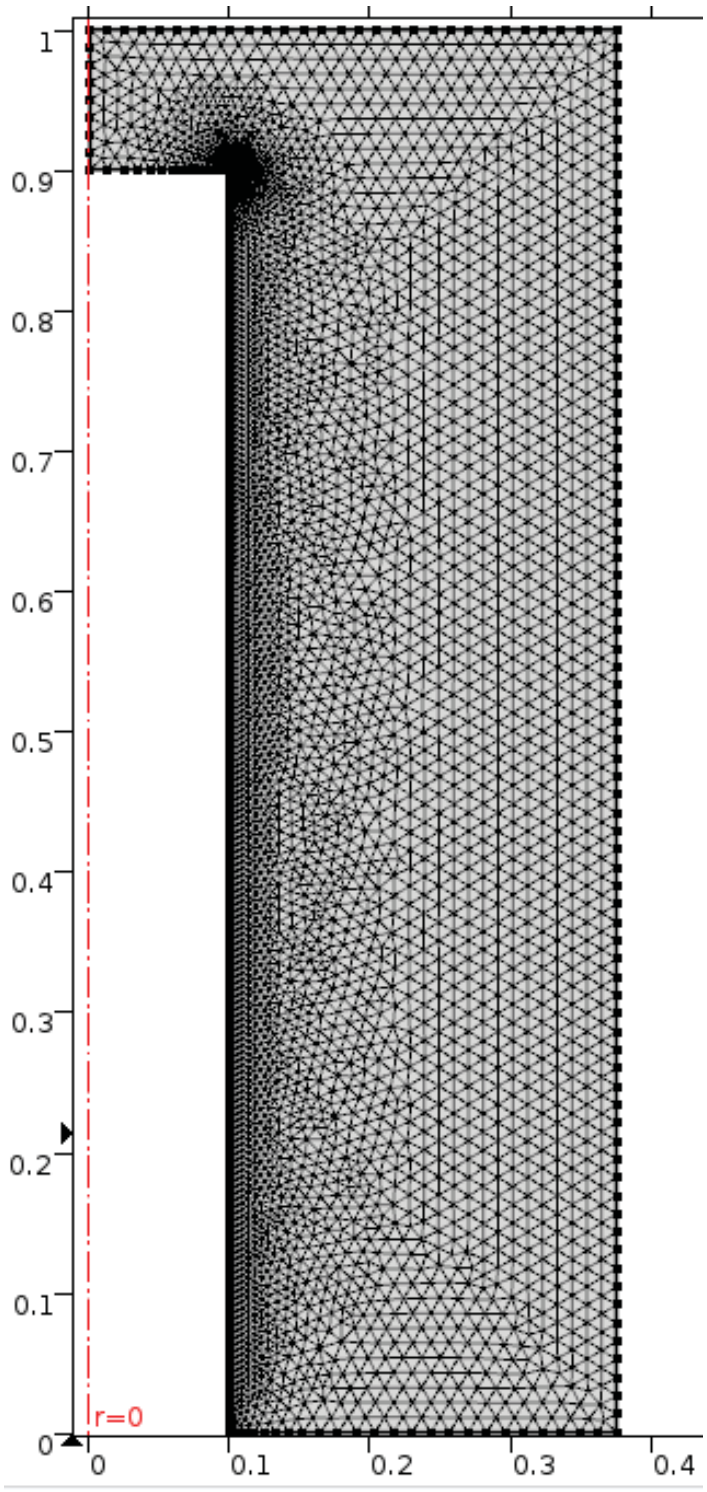

Figure 5-2: Overall mesh of the entire axisymmetric geometry

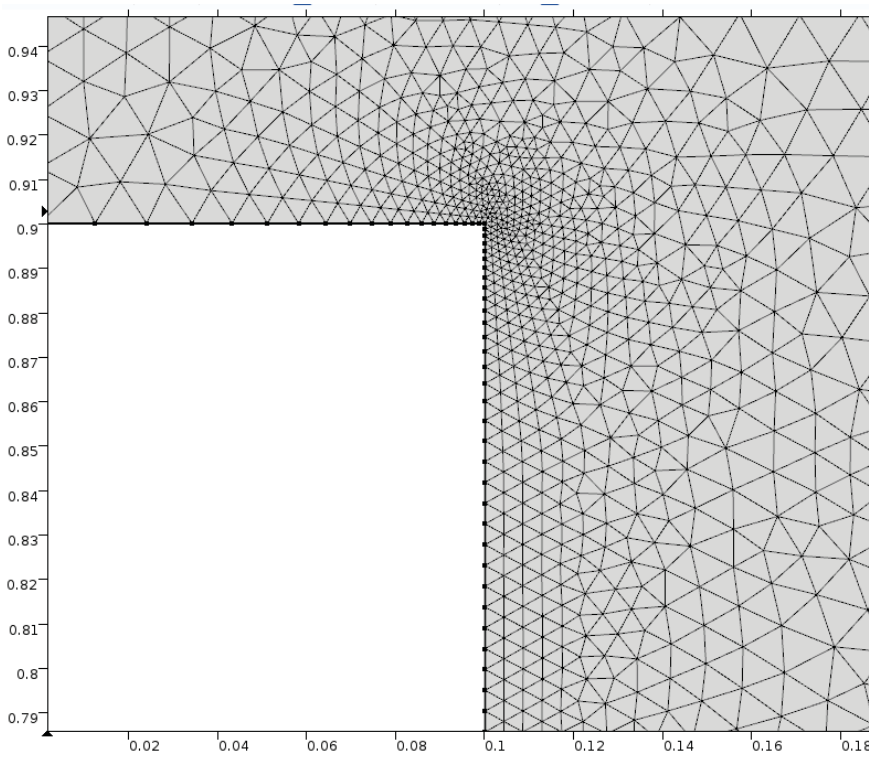

Figure 5-3: Refined meshing across the perforated core boundary, as this is where the most rapid change occurs

Even with these improvements, it was discovered that the meshing was still not suitable as it was producing oscillations in the concentrations of the pyrolysis product yields where the value of tar for example was going below zero, which is impossible. This can be caused by a number of reasons:

1) the physical model is incorrectly set up, the flow of the solver should be set up in such a way that the dependent variables are calculated in a logical order, for example if mass conservation reactions are dependent on temperature, then the variable T should be calculated before the mass conservation equations are solved;
2) the initial conditions are unrealistic i.e. they are too far out for the model to converge;
3) the meshing is too coarse and therefore does not capture the fast dynamics;
4) high convective regime (similar to 3) above);
5) high Damkohler number[4] (similar to 3) and 4) above).

[4] Damkohler number is the ratio of reaction rate to convective mass transport rate and is an estimation for how quickly gases diffuse through a particle or bed of particles.

The easiest way to diagnose this problem was to solve the model with two types of meshes, a coarse and a very fine mesh. If the oscillations improve, then meshing (number 3) can be concluded as the issue, if it does not, then a closer investigation of 1) and 2) would need to be carried out. It was discovered after some trials that the meshing was too coarse, as the oscillations improved with finer mesh sizes, and thus it was concluded that 3) was the cause of the problem and thus a finer mesh was used for the remainder of the calculations. The final meshing used had 7835 domain elements and 357 boundary elements and took approximately 25 minutes to solve for a 3.5-hour total simulation time. This final meshing was chosen as a result of no further improvement in the solution was observed with finer meshing. This time was further reduced to 8-12 minute solving time (depending on parameters), by inputting more accurate initial conditions. These are discussed later in section 6.

It is interesting to observe that the mesh (Fig 5.2) is very fine at the internal perforated core boundary. Here, the pyrolysis gases flow from the reactor into the core then down into the combustion chamber. Flow in the core is not modelled. No reactions occur at the perforated boundary. Therefore, it can be asked ‘why is such a fine mesh needed at this boundary?’. The reason is not entirely known, however is mostly likely due to the presence of the corner at the top of the perforated region, which figure 5.3 shows, requires particularly fine meshing. In retrospect, this ‘corner’ problem may have been avoided by using a hemisphere as the top of the inner perforated core. Also to be noted is that as the pyrolysis front sweeps across the reactor even at this boundary, the rate of change of the system variables is significant.

6. Modeling results & discussion

The model developed was simulated with various initial conditions. The main initial conditions were the heating rate (wall heat flux/temperature) and the permeability of the porous media (bed of wood chips). Permeability is important as it accounts for the particle packing density and configuration and thus has a significant influence on the convective heat and mass transfer of the system.

6.1. Comparison of theoretical model results with experimental results

The following simulation results were computed with the following system parameters, initial conditions and boundary conditions.

Table 6-1: Thermo-physical parameters used in the Model

Symbols	Expression	Units
$C_{P,wood}$	$1.5 + (1.0 \times 10^{-3})T$	kJ kg^{-1} K^{-1}
$C_{P,\ char}$	$0.42 + (2.09 \times 10^{-3})T + (6.85 \times 10^{-3})T^2$	kJ kg^{-1} K^{-1}
$C_{p,\ volatiles}$	$-0.10 + (4.40 \times 10^{-3})T - (1.57 \times 10^{-6})T^2$	kJ kg^{-1} K^{-1}
κ_{wood}	0.35	W m^{-1} K^{-1}
κ_{char}	0.10	W m^{-1} K^{-1}
κ_{tar}	0.0258	W m^{-1} K^{-1}
$d_{pore,\ wood}$	5.0×10^{-5}	m
$d_{pore\ char}$	1.0×10^{-4}	m
ε_{wood}	0.7	(-)
ε_{char}	0.92	(-)
K	2.5×10^{-6}	m^2
$\mu_{volatiels}$	$(-3.73 \times 10^{-7}) + (2.62 \times 10^{-8})T$	kg m s^{-1}
M_{water}	18	g mol^{-1}
M_{tar}	110	g mol^{-1}
M_{gas}	36	g mol^{-1}
P_{atm}	1.01325×10^5	N m^{-2}/Pa
$T_{initial}$	20	°C
σ	5.6703×10^{-8}	W m^{-2} K^{-4}

Initial Conditions & Parameters

Pyrolysis in a pilot scale cylindrical batch reactor of height 1000 mm and radius 275 mm has been simulated. The initial pressure, temperature and moisture content are 293.15 K (20°C), 0.8 atm. (81,060 Pa (N m^{-2})) and 5% wt., respectively. The total time of the simulation is 14,400 seconds or 3.5 hours, which is the time it took for pyrolysis to reach completion in the experimental pilot scale set-up. Model thermo-physical properties are contained in table 6-1.

There are limited experiments that have been conducted for pyrolysis at a large scale. There are some works done for 1-2 cm diameter wood cylinders by (Lee, Chaiken, Singer 1976) and (Chan, Kelbon and Krieger, 1985). However, the physical and chemical phenomena at these relatively small scales are very different to those of this pilot scale model with a radius of 275 mm. Therefore, in order to validate this model, the only reasonable approach was to directly compare the model data to the experimental data of this particular rig. For this experimental set-up, only two parameters were monitored during runs. The centre temperature was measured using a thermocouple that was placed in the centre of the perforated core and the flue gas temperature was monitored at the bottom of the flue stack. The furnace temperature was indicative of the outer wall temperature of the reactor and was later used for that purpose. However the first simulation assumed a first order increase in wall temperature to 650 °C. The centre temperature was used for model comparison.

Figure 6.1 below shows the plot of time vs. temperature for a particular run where 70 kg of wood chips were packed inside the reactor (0.44 m^3). The maximum temperature reached during the run was 650 °C and so this was used as the boundary wall temperature of the simulation. Two simulations were performed, the first using Fantozzi (2007) kinetics and a second, with modified kinetics to obtain a better fit. When using the Fantozzi kinetic approach, the temperature at which the primary reactions begin is slightly higher at 240 °C, compared to that shown by the experimental at 180 °C. This is because the kinetic parameters used were experimentally obtained for poplar wood and not pine. By modifying the kinetic parameters, it was possible to obtain a much closer prediction of the temperature profile as shown by the dashed line.

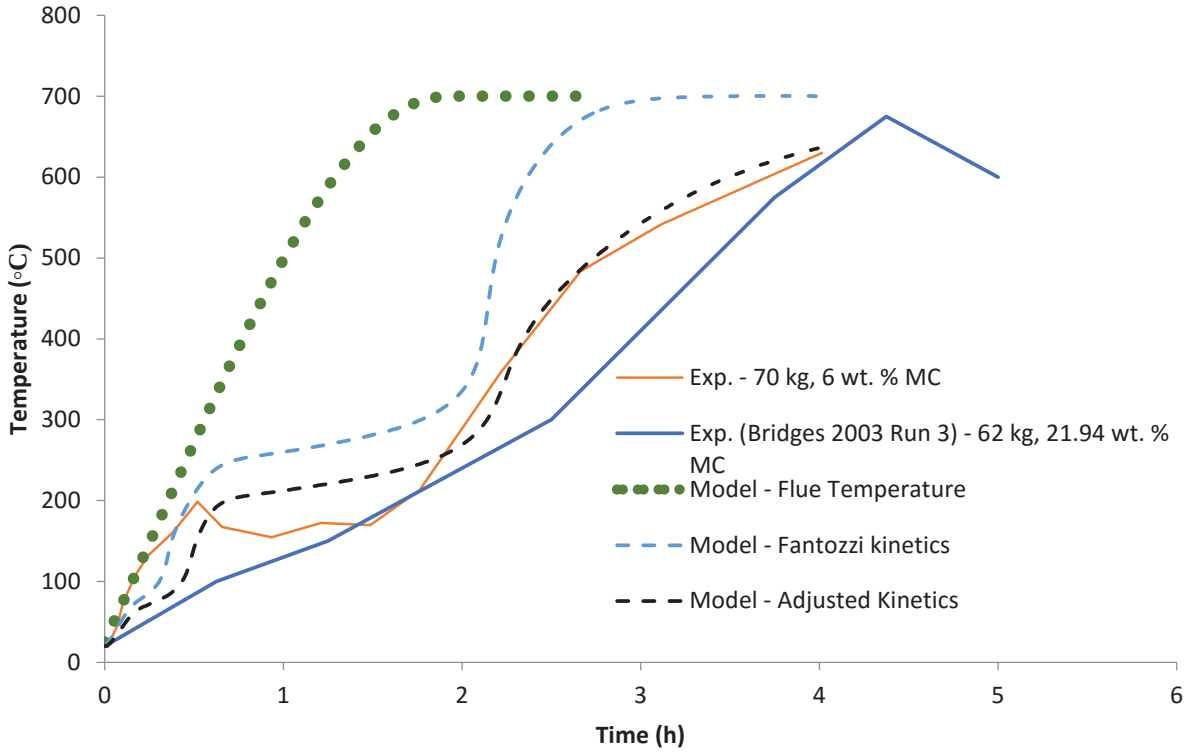

Figure 6-1: Validation of centre temperatures at a wall temperature of 650°C showing comparison between Fantozzi kinetics for poplar, tuned pine parameters per table 4-1. The wall temperature used in the model is the experimental temperature measured at the bottom of the stack. The experimental data was collected as described in Appendix D.

After a satisfactory profile fit, the model can now be used to make predictions and to analyse other variables that would otherwise be too difficult or time consuming to investigate experimentally.

The objectives of this research included being able to produce a model that would accurately predict the biochar yield, quality and time of completion of the runs. Time of completion is considered the point at which the centre temperature reaches the desired peak treatment temperature (PTT). As shown by Figure 6.2 below, the time of completion is highly dependent on heating rate and PTT. The fastest time for completion (100% of Wood is consumed) is when the PTT is 700°C, and the time taken is just under 3 hours. While the longest time for completion is when the PTT is 400°C, and it takes almost 4 hours for the pyrolysis reactions to come to completion.

6.1.1. Biochar yield and quality

According to literature (discussed by Bridges, 2013) biochar yield is highly dependent on peak treatment temperature (PTT) and heating rate. Simulations were therefore conducted at different peak wall temperatures, which were all ramped up at the same first order rate shown in figure 6-1.The range of temperatures studied were 400°C-700°C in order to evaluate whether the model correlation to the experimental data. Figure 6.2 below shows the centre temperature profiles for these simulations and Table 6-2 has the biochar yields. These yields were determined at a single node selected to be that which was furthest from all heating surfaces, i.e., it was against the perforated core half way up the reactor. This node was selected because it experiences the slowest heating rate and therefore will give the highest yield of all nodes within the reactor. While this was true, all other nodes showed very similar yields (to the third significant figure, results not shown) because the reactions occur slowly, over many hours. Therefore, the selection of a node is a matter of rigour rather than accuracy.

Table 6-2: Biochar yields predicted by the model for a range of peak treatment temperatures

Peak Treatment Temperature (°C)	400	500	600	700
Biochar Yield (Dry Basis, wt.%)	28.20%	26.86%	26.13%	25.67%

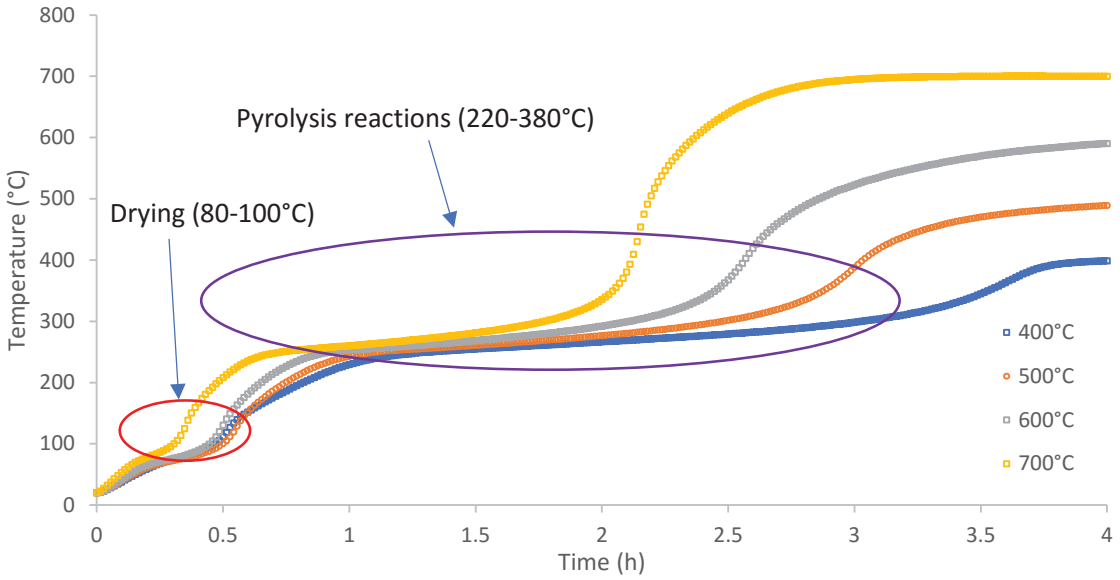

Figure 6-2: Centre Temperature profile for different wall temperatures (400-700°C)

The experimental results published by Bridges, et al. (2013) showed a similar correlation to the model. As PTT increased, biochar yield decreased. At 400 °C peak treatment temperature, experimental yields were in the range of 32-35%, slightly higher than the predicted results from the simulation of 28.2% and at a PTT of 700°C, the experimental yield was in the range of 19-25%, while the model predicted a maximum yield of 25.67%. While the experimental range is greater, the trend is the same, and so it provides assurance that the model can be used to approximate biochar yield, considering all other factors, such as particle size and operating conditions remain the same. Bridges experimental results are also exposed to factors that are not considered in a simplified model. At low temperatures Bridges found that the extent of pyrolysis was not uniform throughout the reactor and at high temperatures the effect of minor air ingress during the larger cool down phase, may have contributed to some oxidation, lowering of the yield.

Peak treatment temperature was also shown to highly correlate with other characteristics of bio-char, such as volatile matter, fixed carbon and elemental components such as nitrogen, hydrogen, carbon and oxygen. Although these cannot be confirmed by the model, it is possible

to assume that the biochar quality can be predicted based on the model's ability to predict biochar yield and temperature profile.

Volatile matter content is shown to decrease with increased PTT. This can explain the decrease in over-all biochar (solid) yield at higher treatment temperatures, as more of the volatile matter is driven off at those temperatures. According to Bridges, et al. (6), a PTT of 600°C must be achieved in order to produce biochar with less than 10% wt. volatile matter content, this does not decrease much with further heating, and therefore to conserve energy, pyrolysis in this reactor should not be run at higher than 600°C. Although due to the nature of the process being exothermic when secondary reactions begin, the peak temperature is uncontrollable.

Although not captured in the model, fixed carbon content is also highly correlated to the PTT (Grønli, 1996). As more volatile content is driven off, fixed carbon becomes a higher percentage of the leftover solid. Similar to the volatile matter content, fixed carbon does not increase much after 600°C and therefore it can be assumed that the optimum operating temperature for pyrolysis in order to produce stable biochar is 600°C. This will consume the least amount of energy and time, while producing a biochar with reasonably low volatile matter content and high fixed carbon content, making it optimum for carbon sequestration. While fixed carbon and volatile matter content are ways to predict biochar quality, another method is to compare the oxygen to carbon ratio against the hydrogen to carbon ratios of the biochar, on a plot known as the Van Krevelen Diagram which is typically used to quantify coal quality. The correlation for this is also highly dependent on PTT. The experiments conducted by Bridges et al. (6) showed that the optimum PTT for production of high quality biochar (Low H/C to O/C ratios) was again, biochar produced at a PTT of 600°C. Biochar produced at 700°C did not show any significant increase in biochar quality. For comparison purposes, biochar produced in this reactor at a temperature of 600°C had a H/C ratio of 0.25 and an O/C ratio of 0.025. Bituminous coal has a H/C ratio of anywhere between 0 and 0.75 and an O/C ratio of 0 to 0.05.

In summary, the model predicts char yields that are in the same range and follow the same trends as that observed experimentally by Bridges (2013). While the model does not predict char quality parameters of fixed carbon content, volatile matter content or elemental H/C ratio,

these parameters all relate directly to the peak treatment temperature, which is a controlled parameter in the model. Therefore, the model describes pyrolysis adequately for the purpose of determining the heating profile, the time to completion and the production yields of char and volatiles.

6.1.2. Modification of Fantozzi Kinetics

The model, as described above, used modified kinetics to improve the fit between prediction and experimental results (Figure 6.1). It also used a first order increase in the wall temperature that drives the heat transfer. This section describes why the Fantozzi Kinetics (2007) needed modifying and provides further refinement of the wall heating profile. While the model predicts the experiment results shown in Figure 6.1, the ensuing prediction in figure 6.2 show that pyrolysis occurs at a similar temperature in the 240-300°C range, for all driving wall temperatures, 400-700°C. This indicates that the endothermic primary reactions dominate pyrolysis. However, the work of Bridges (Bridges, 2013) showed that this is not the case. Bridges (Bridges, 2013) found that the pyrolysis is more exothermic than expected.

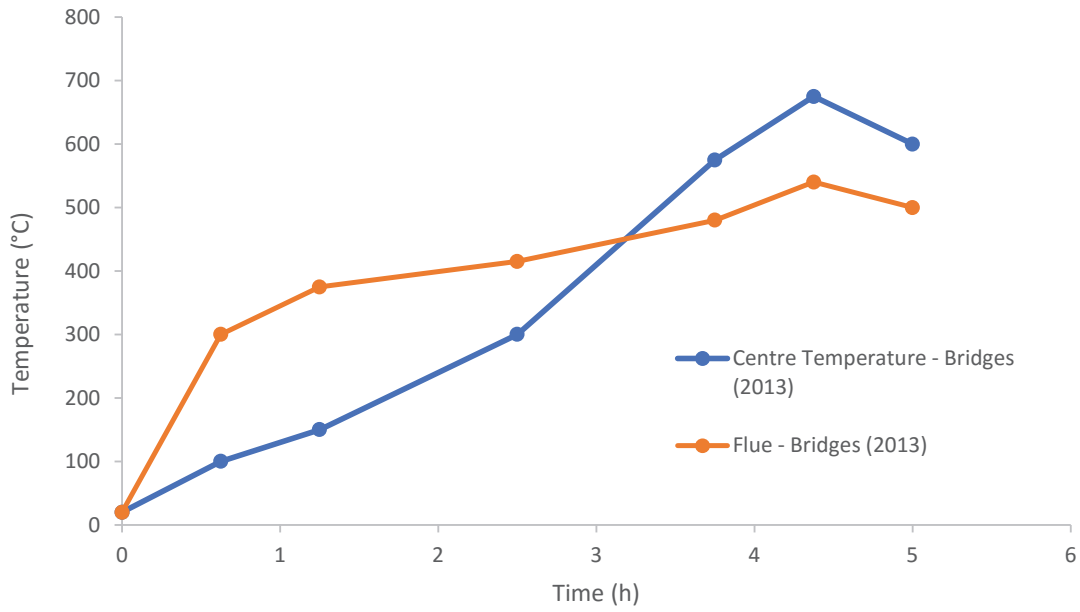

Figure 6-3: Re-produced graph of Run 3 from Bridges (Bridges, 2013)

Figure 6.3 above gives the data for run 3 of Bridges work, showing the reactor centre temperature and flue temperature. This run was done using 62 kg of air dried *Pinus radiata* wood chips of 21.94% moisture content. Several features of the plot can be discussed, although it is apparent that across the reactor evaporation, sensible heating, primary reactions and secondary reactions are occurring simultaneously. First, the reactor core (centre) temperature slows down when water evaporation occurs just above 100°C, followed by sensible heating which then becomes steeper after ~180°C when primary pyrolysis begins then steeper again as secondary reactions dominate. While ~180°C seems low for pyrolysis, it must be remembered that this is the core temperature. The temperature of the wall indicated by the stack temperature, pyrolysis will have started in the near-wall region after ~30 minutes (~280°C) when the core temperature was ~100°C and still recording moisture evaporation. This lag is due to the cycling of volatilisation and condensation of both water vapour and the condensable volatiles as they move towards the reactor core. The steep jump in core temperature after water evaporation is complete is a feature of Bridges experimental work. The precise reason for this is not known, but is likely to be a combined effect of the sensible heating regime without

the suppression by latent heat required for evaporation and the onset of pyrolysis in the near-wall region around 300°C.

The second noteworthy feature which supports exothermicity is the interesting fact that after ~200°C, the core temperature increases at a much faster rate than the stack temperature. This indicates that exothermic reactions are causing this increase. The lower stack temperature is due to the secondary air which enters the combustion chamber. Although it is used to partially combust the pyrolysis gas, it also cools the annular region, apparently because the added heat from partial combustion is insufficient to heat the secondary air which enters at ambient conditions. Other heat losses such as from the outer drum to the air are minimal as the drum is insulated in a 25 mm layer of Superwool plus insulation (The outer surface is hot but not dangerous to light touch, i.e., ~60°C when the flue temperature is ~500°C). The cross over occurs from 440°C after which the reactor core is hotter than the stack. This can only be due to exothermicity. Fantozzi et al. (2007) kinetics do not capture this exothermicity where the heat of reaction of the secondary reactions, tar -> $char_2$ and tar -> gas_2, is set at – 42 kJ kg^{-1} compared to 420 kJ kg^{-1} for the endothermic primary reactions. While the primary heat of reactions is relatively well established, the secondary heat of reaction is worth exploring.

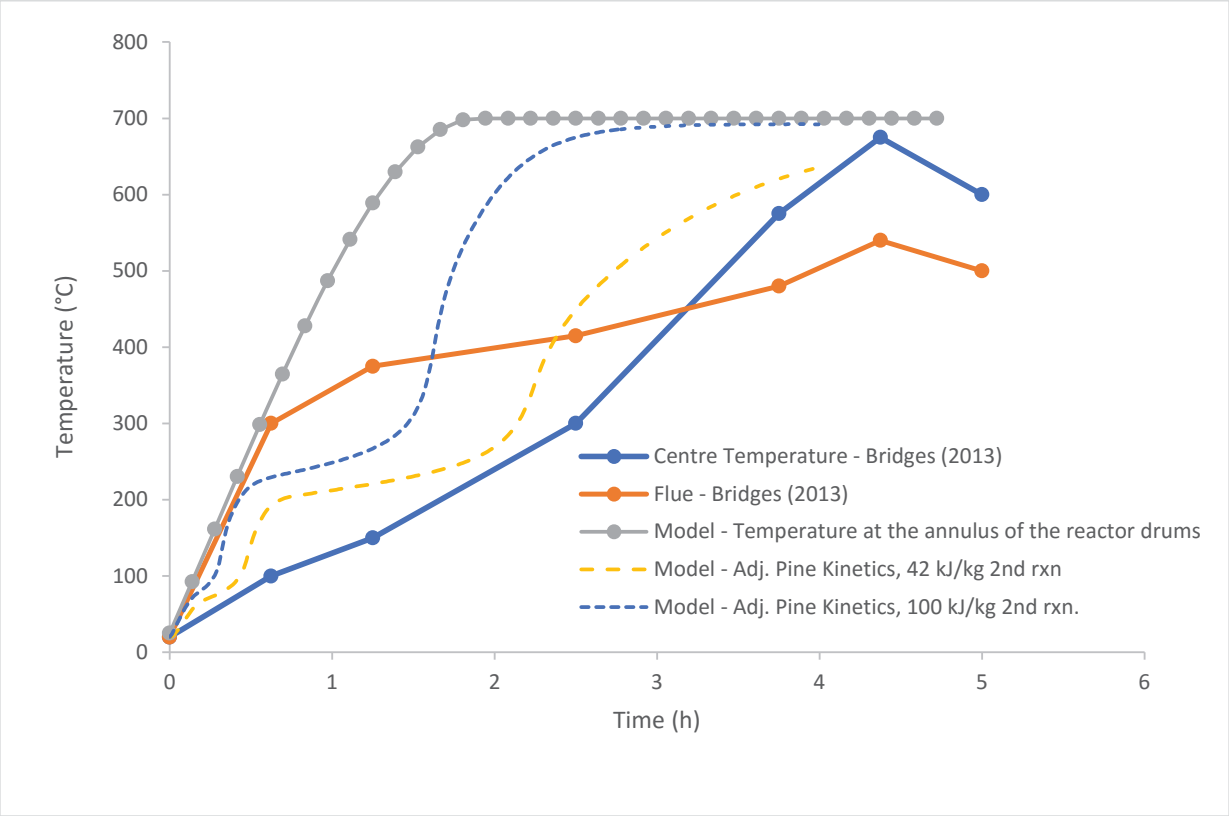

Figure 6-4: Effect of exothermicity on temperature profile compared to Run 3 from Bridges work (Bridges, 2013)**. (2nd = Secondary, rxn = reactions). The model assumes the bottom of the annulus 200°C (section 4) hotter than the bottom of the flue stack, thus the flue temperature of the model is comparable to that of Bridge's experimental peak value of ~500°C.**

Figure 6.4 above compares two secondary heats of reaction, Fantozzi et al. (2007) at -42 kJ mol^{-1}, and -100 kJ mol^{-1}, while still retaining an assumed first order increase in reactor wall temperature. While this wall temperature is clearly not observed by Bridges, it isolates the effect of having more exothermicity in the secondary reactions. The result is that the system temperature increases more quickly. It must be noted that the core temperature does not exceed the model wall temperature, but this is most likely because it does not represent the experimental system.

6.1.3. Sensitivity analysis of decomposition reaction properties

The effect of the other pyrolysis reaction kinetic parameters was investigated to see how it influences the outcomes. Reaction kinetics for the 5 reactions were altered ±5% (one reaction at a time). Due to what is commonly known as the compensation effect (Strongly coupled activation energy and Frequency factor) when dealing with Arrhenius kinetics, the following relation was used to calculate the new parameters:

$$A = A_{ref} \exp\left[\frac{E - E_{ref}}{RT_{iso}}\right] \tag{6.1}$$

Where A_{ref}, E_{ref} and A and E are the reference and new frequency factor and activation energy, respectively. These are all references to a common temperature, T_{iso} = 591 K (318°C) (Grønli, 1996).

Table 6-3: New Kinetic Reaction parameters used for the effect of decomposition reaction study

	A [1/s]			E [J/mol]		
Reactions	0	5%	-5%	0	5%	-5%
Gas reaction	1.44×10^4	3.55×10^4	5.85×10^3	88,600	93,030	84,170
Tar reaction	4.13×10^6	1.30×10^7	1.31×10^6	112,700	118,335	107,065
Char reaction	7.38×10^5	2.18×10^6	2.50×10^5	106,500	111,825	101,175
2nd. Gas reaction	4.28×10^6	1.28×10^7	1.43×10^6	107,500	112,875	102,125
2nd. Char reaction	1.00×10^5	2.99×10^5	3.35×10^4	107,500	112,875	102,125

In this research, biochar yield is the most important parameter to predict as both tar and non-condensable gases are flared off in the reactor and thus are not collected or measured. The following table 6.4 shows the effect of changing the kinetic parameters on the biochar yield.

Table 6-4: Effects of kinetic parameters on biochar yield

	Biochar yield				
Parameter Change	**5%**	**Difference**	**Stock Fantozzi**	**-5%**	**Difference**
Gas reaction	27%	1%	28%	25%	3%
Tar reaction	26%	2%	28%	26%	3%
Char reaction	26%	2%	28%	26%	2%
Sec. Gas reaction	26%	2%	28%	26%	2%
Sec. Char reaction	26%	2%	28%	26%	2%

Increasing the gas reaction rate reduced the char yield by 1% while decreasing the rate decreased the yield by 3%. This was the most significant change in the char yield, the reaction rates of other species had a similar change in char yield whether the rate was decreased or increased.

7. Conclusions and future research

There were two objectives for this research project

1) Modify the existing flare system of the pyrolyser so that the emissions produced are within US and NZ EPA limits.
2) Develop a comprehensive mathematical model that can be used to predict temperature profile, biochar yield and biochar quality.

Compliance

The reactor originally had problems with fugitive emissions and the inability to properly flare pyrolysis gases. Fugitive emissions were caused by a slight over pressure in the system especially during peak pyrolysis reaction rates (240-450°C centre temperature). This caused gases to leak through, especially around the lid and combustion chamber. The issue with the lid was that it would expand unevenly during heating which created small gaps around the rim where pyrolysis gases were able to leak out. In order to address the issue of uneven expansion, the material of the lid was changed from sheet metal stainless steel, to fire brick cement. The fire brick cement has a negligible expansion rate when heated compared to the steel. The combustion chamber was also sealed more thoroughly with thick ceramic insulation rope.

The flare was also ineffective in dealing with the pyrolysis gases that were being released. Due to the nature of biomass such as wood, the pyrolysis gases produced contain large concentrations of inert gases such as H_2O and CO_2.

A new flare system was designed and installed. The new system had three times as much power as the original, which utilised a single 3.4 kW pilot burner. The pilot burners were installed at the very top of the flue stack; this is to allows the pyrolysis gases to mix with the air before combusting. A dedicated blower was also installed to force air into the flare zone so that the pilot burners always have an adequate supply of oxygen and so that the pilot burners do not blow out due to poor combustion.

The above mentioned modifications are yet to be tested. Due to the extra weight of the components installed for the new flare system, the opening and closing mechanism of the pyrolyser was compromised and therefore a new system to open and close the pyrolyser for filling and emptying had to be designed and built. This is currently in progress. Once emissions compliance is established, the reactor design will be made publicly available. It is the intention that this design is open source.

Modelling

An axisymmetric mechanistic model for the simultaneous heat and mass transfer in porous media has been developed to simulate wood chip pyrolysis in a large scale batch reactor, with diameter 750 mm and height 1000 mm. The details are described within this thesis and that of Bridges (2013). The main objectives of the model are to predict time of completion for a run, temperature profile, and biochar yield and quality. Comparing the temperature profile and thus the heating rate of the experimental results with the model produced a satisfactory agreement after adjusting pyrolysis kinetic parameters of poplar wood to better reflect those of pine wood, which is the wood species used in this project.

Pyrolysis products are highly influenced by heating rate and maximum holding temperature. Biochar yields were compared at different peak wall temperatures. Model results showed the same trend and fell in the same range as experimental results, that is, the highest holding temperature caused biochar yields to decrease.

Overall, the results of this model provide valuable information on the fixed bed pyrolysis of pine wood chips (Pinus radiata) which is the feedstock used in this project. This knowledge can be utilised for the optimization of batch reactor and can easily be used to predict the product and temperature profile reaction time, and char yield. It was shown how peak temperature and char yield relate to char qualities, although the specifics of char quality, the fixed carbon content, volatile matter content and elemental H/C ratio are not individually able to be predicted. The model canbe usefully applied to other feedstocks (e.g. corn stover, wheat straws and other biomass) by simply changing material properties.

8. References

Abdel-Shafy, H. I. and Mansour, M. S. M. (2015) 'A review on polycyclic aromatic hydrocarbons: Source, environmental impact, effect on human health and remediation', *Egyptian Journal of Petroleum*. Egyptian Petroleum Research Institute, 25(1), pp. 107–123. doi: 10.1016/j.ejpe.2015.03.011.

Al., F. et (2007) 'Rotary Kiln Slow Pyrolysis for Syngas and Char Production From Biomass and Waste — Part I : Working Envelope of the Reactor Rotary Kiln Slow Pyrolysis for Syngas and Char Production From Biomass and Waste — Part I : Working Envelope of the Reactor', (August 2016). doi: 10.1115/1.2720521.

Antal, M. J. and Grønli, M. (2003) 'The Art, Science, and Technology of Charcoal Production', *Industrial & Engineering Chemistry Research*, 42(8), pp. 1619–1640. doi: 10.1021/ie0207919.

Bamford, C. H. *et al.* (1946) 'The combustion of wood. Part I', *Mathematical Proceedings of the Cambridge Philosophical Society*, 42(2), p. 166. doi: 10.1017/S030500410002288X.

Bellais, M. (2007) *Modelling of the pyrolysis of large wood particles*. doi: 10.1016/j.biortech.2009.01.007.

Di Blasi, C. (1993) 'Modeling and simulation of combustion processes of charring and non-charring solid fuels', *Progress in Energy and Combustion Science*, 19(1), pp. 71–104. doi: 10.1016/0360-1285(93)90022-7.

Di Blasi, C. (1996) 'Heat, momentum and mass transport through a shrinking biomass particle exposed to thermal radiation', *Chemical Engineering Science*, pp. 1121–1132. doi: 10.1016/S0009-2509(96)80011-X.

Blasi, C. Di (2000) 'Modelling the fast pyrolysis of cellulosic particles in # uid-bed reactors', 55.

Di Blasi, C. (2008) 'Modeling chemical and physical processes of wood and biomass pyrolysis', *Progress in Energy and Combustion Science*, 34(1), pp. 47–90. doi: 10.1016/j.pecs.2006.12.001.

Bridges, R. (2013) *Design and Characterisation of an 'Open Source' Pyrolyser for Biochar Production*. Massey University.

Bridges, R. P., Paterson, A. H. J. (Tony. and Jones, J. R. (2013) 'Design and Characterisation of an "Open Source" Pyrolyser for Biochar Production', *Conference.Net.Au*.

Bruchmu¨ller, J. *et al.* (2011) 'Modeling the Thermochemical Degradation of Biomass Inside a Fast Pyrolysis Fluidized Bed Reactor', *American Institute of Chemical Engineers*, 0(0), pp. 1–13.

Caine, M. (2000) 'Biogas Flares', *Technology*, (December).

Chan, R. and Krieger, B. B. (1983) 'Modeling of Physical and Chemical Processes During Pyrolysis of a Large Biomass Pellet With Experimental Verification.', *ACS Division of Fuel Chemistry, Preprints*, 28(5), pp. 330–337.

Chan, W.-C. R., Kelbon, M. and Krieger, B. B. (1985) 'Modelling and experimental verification of physical and chemical processes during pyrolysis of a large biomass particle', *Fuel*, 64(11), pp. 1505–1513. doi: 10.1016/0016-2361(85)90364-3.

Chen, D., Zhou, J. and Zhang, Q. (2014) 'Effects of heating rate on slow pyrolysis behavior, kinetic parameters and products properties of moso bamboo', *Bioresource Technology*. Elsevier Ltd, 169, pp. 313–319. doi: 10.1016/j.biortech.2014.07.009.

Corbetta, M. *et al.* (2014) 'Pyrolysis of centimeter-scale woody biomass particles: Kinetic modeling and experimental validation', *Energy and Fuels*, 28(6), pp. 3884–3898. doi: 10.1021/ef500525v.

Dayton, D. C. *et al.* (1999) 'Release of Inorganic Constituents from Leached Biomass during Thermal Conversion', 1977(2), pp. 860–870.

Evans, R. J. and Milne, T. A. (1987a) 'Molecular characterization of the pyrolysis of biomass 1. Fundamentals', 1(2).

Evans, R. J. and Milne, T. A. (1987b) 'Molecular characterization of the pyrolysis of biomass 2. Applications', 1(4), pp. 311–319.

Fantozzi, F. *et al.* (2007) 'Rotary Kiln Slow Pyrolysis for Syngas and Char Production from Biomass and Waste Part 2: Introducting product yields in the energy balance', pp. 908–913.

Forest Products Laboratory (2010) 'Wood Handbook: Wood as an Engineering Material', *Agriculture*, 72, p. 466. doi: General Technical Report FPL-GTR-190.

Grønli, M. G. (1996) *Gronli 1996 PhD Thesis - Norwegian Univ of Science and Technology - A Theoretical and Experimental Study of the Thermal Degradation of Biomass.pdf*. The Norwegian University of Science and Technology.

Grønli, M. G., Várhegyi, G. and Di Blasi, C. (2002) 'Thermogravimetric Analysis and Devolatilization Kinetics of Wood', *Industrial & Engineering Chemistry Research*, 41(17), pp. 4201–4208. doi: 10.1021/ie0201157.

Hagge, M. J. and Bryden, K. M. (2002) 'Modeling the impact of shrinkage on the pyrolysis of dry biomass', *Chemical Engineering Science*, 57(14), pp. 2811–2823. doi: 10.1016/S0009-2509(02)00167-7.

Hsu, C. T. and Cheng, P. (1990) 'Thermal dispersion in a porous medium', *International journal of heat and mass transfer*, 33(8), pp. 1587–1597.

Incropera, F. P. *et al.* (2006) *Fundamentals of Heat and Mass transfer*. 6th edn. John Wiley & Sons.

Janssens, M. and Douglas, B. (2004) 'Wood and Wood Products', in *Handbook of Building Materials for Fire Protection*. New York: McGraw-Hill, pp. 1–58.

Koch, P. (1968) 'Specific heat of ovendry spruce pine wood and bark', *Wood Science*, 1(4), pp. 2013–214. Available at: https://www.srs.fs.fed.us/pubs/24101.

Laird, D. A. *et al.* (2010) 'Impact of biochar amendments on the quality of a typical Midwestern agricultural soil', *Geoderma*. Elsevier B.V., 158(3–4), pp. 443–449. doi: 10.1016/j.geoderma.2010.05.013.

Lam, K. L., Oyedun, A. O. and Hui, C. W. (2012) 'Experimental and Modelling Studies of Biomass Pyrolysis *', 20(3), pp. 543–550.

Lehmann, J. (2007) 'Bio-energy in the black', *Front Ecol Environ*, 5(7), pp. 381–387.

Lehmann, J. *et al.* (2011) 'Biochar effects on soil biota - A review', *Soil Biology and Biochemistry*. Elsevier Ltd, 43(9), pp. 1812–1836. doi: 10.1016/j.soilbio.2011.04.022.

Lehmann, J. and Joseph, S. (2009) 'Biochar for Environmental Management : An Introduction', *Science And Technology*, 1, pp. 1–12. doi: 10.1016/j.forpol.2009.07.001.

Liden, A. G., Berruti, F. and Scott, D. S. (1988) 'A kinetic model for the production of liquids from the flash pyrolysis of biomass', *Chemical Engineering Communications*, 65, pp. 207–221.

Mamleev, V., Bourbigot, S. and Yvon, J. (2007) 'Kinetic analysis of the thermal decomposition of cellulose: The main step of mass loss', *Journal of Analytical and Applied Pyrolysis*, 80(1), pp. 151–165. doi: 10.1016/j.jaap.2007.01.013.

McCabe, W. L., Smith, J. C. and Harriott, P. (2005) *Unit Operations of Chemical Engineering*. 7th edn. New York: McGraw-Hill.

Mcgrath, J. F., Copeland, B. and Dumbrell, I. C. (2002) 'Magnitude and duration of growth and wood quality responses to phosphorus and nitrogen in thinned Pinus radiata in southern Western Australia', *Australian Forestry*, 66(3), pp. 223–230. doi: 10.1080/00049158.2003.10674916.

Morf, P., Hasler, P. and Nussbaumer, T. (2002) 'Mechanisms and kinetics of homogeneous secondary reactions of tar from continuous pyrolysis of wood chips', *Fuel*, 81(7), pp. 843–853. doi: 10.1016/S0016-2361(01)00216-2.

Mukhopadhyaya, P. *et al.* (2002) 'Effect of surface temperature on water absorption coefficient of building materials', *thermal envelope and building science*, 26(2), pp. 179–195.

Nield, D. A. and Bejan, A. (2013) 'Convection in porous media', *Convection in Porous Media*, pp. 1–778. doi: 10.1007/978-1-4614-5541-7.

NIST Chemistry WebBook (2016) *National Institute of Standards and Technology*. Available at: http://webbook.nist.gov/chemistry/ (Accessed: 1 May 2016).

O'Neill, B. *et al.* (2009) 'Bacterial community composition in Brazilian Anthrosols and adjacent soils characterized using culturing and molecular identification', *Microbial Ecology*, 58(1), pp. 23–35. doi: 10.1007/s00248-009-9515-y.

Park, W. C., Atreya, A. and Baum, H. R. (2009) 'Experimental and theoretical investigation of heat and mass transfer processes during wood pyrolysis', *Combustion and Flame*, pp. 481–494. doi: 10.1016/j.combustflame.2009.10.006.

Pew, J. C. (1952) 'The chemistry of lignin', *Journal of Colloid Science*, 7(6), pp. 648–649. doi: 10.1016/0095-8522(52)90050-0.

Ratte, J. *et al.* (2009) 'Mathematical modelling of slow pyrolysis of a particle of treated wood waste', *Journal of Hazardous Materials*, 170(2–3), pp. 1023–1040. doi: 10.1016/j.jhazmat.2009.05.077.

Ratte, J. *et al.* (2009) 'Mathematical modelling of slow pyrolysis of a particle of treated wood waste', 170, pp. 1023–1040. doi: 10.1016/j.jhazmat.2009.05.077.

Raznjevic, K. (1975) *Handbook of Thermodynamic Tables and Charts*. Edited by H. B. Crawford. Washington: Hemisphere Publishing Corporation-McGraw Hill.

Richards, G. (2004) 'A modelled carbon account for Australia's post-1990 plantation estate', *Australian Forestry*, 67(4), pp. 289–300. doi: 10.1080/00049158.2004.10674949.

Scott, D. S., Piskorz, J. and Radlein, D. (1985) 'Liquid products from the continuous flash pyrolysis of biomass', *Industrial & Engineering Chemistry Process Design and Development*, 24(3), pp. 581–588. doi: 10.1021/i200030a011.

Shafizadeh, F. and Chin, P. P. S. (1977) 'Thermal deterioration of wood', in *Wood Technology: Chemical Aspects*, pp. 57–81.

Slattery, J. C. (1967) 'Flow of viscoelastic fluids through porous media', *AIChE Journal*, 13(6), pp. 1066–1071. doi: 10.1002/aic.690130606.

Sombroek, W. G. *et al.* (2003) 'Amazonian dark earths as carbon stores and sinks', *Amazonian Dark Earths: Origins, Properties, Management.*, pp. 125–139. doi: 10.1007/1-4020-2597-1_7.

Thurner, F. and Mann (1981) 'Kinetic investigation of wood pyrolysis', *Industrial & Engineering Chemistry Process Design and Development*, 20, pp. 482–488. doi: 10.1021/i200014a015.

Whitaker, S. (1967) 'Diffusion and Dispersion in Porous Media', *A. I. Ch. E. Journal*, 13(3), pp. 420–427.

Woodstairs (2012) *WoodStairs*, *www.woodstairs.com/tradepage/2012/07*.

WorkSafe (2016) *Workplace Exposure Standards and Biological Exposure Indices*.

Yagi, S. and Kunii, D. (1957) 'Studies on effective thermal conductivities in packed beds', *American Institute of Chemical Engineers*, 3(3), pp. 373–381.

Yang, H. *et al.* (2007) 'Characteristics of hemicellulose, cellulose and lignin pyrolysis', *Fuel*, 86(12–13), pp. 1781–1788. doi: 10.1016/j.fuel.2006.12.013.

9. Appendix

9.1. Appendix A

Dimensions of the reactor

Radius = 375 mm

Height = 1000 mm

Dimensions of perforated core

Radius = 100 mm

Height = 900 mm

Volume of reactor

$$V_{cylinder} = \pi r^2 h$$

$$V_{total} = V_{reactor} - V_{perforated\ core}$$

$$V_{reactor} = \pi \cdot (.375^2)(1) = 0.44\ m^3$$

$$V_{perforated\ core} = \pi \cdot (.1^2)(.9) = 0.028\ m^3$$

$$V_{total} = 0.44 - 0.028 = 0.412\ m^3$$

$\pi = 3.14 \ldots (constant)$

$r = radius, m$

$h = height, m$

Mass of wood chips

Case 1: 70 kg (full)

Case 2: 46 kg (2/3 full)

Case 3: 35 kg (1/2 full)

Porosity

$$\varphi = Porosity = \frac{void\ space}{total\ space}$$

$$\rho_{wood} = 480 \frac{kg}{m^3}$$

$$V_{solid} = 1 - \frac{70\ kg}{480 \frac{kg}{m^3}} = 1 - 0.146\ m^3$$

$$\varphi = 1 - \left(\frac{V_{solids}}{V_{total}}\right) = 1 - \left(\frac{0.146}{0.412}\right) = 0.646 = 0.65$$

Carmen-Kozeny Equation

$$K = \frac{\varphi^3 D_s^2}{180(1-\varphi)^2}$$

Figure 0-1: Carmen-Kozeny relationship for estimation of Permeability of packed bed of porous material

Where,

K = Permeability, m^2

φ = Porosity, (-)

D_s = Diameter of particles, m

Average dimensions of wood chip:

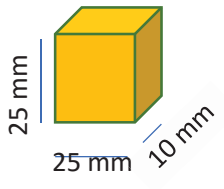

$$V_{wood-chips} = Width \cdot Length \cdot Height$$

$$V_{wood-chips} = 0.025 \cdot 0.025 \cdot 0.01 = 6.25 \times 10^{-6} m^3$$

$$V_{sphere} = \frac{4}{3}\pi r^3$$

$$re - arrange\ for\ r\ to\ find\ equivalent\ diameter\ of\ a\ non - uniform\ particle$$

$$r = \sqrt[3]{\frac{3 \cdot 6.25 \times 10^{-6}}{4\pi}} = 0.011427.. = 1.143 \times 10^{-2} m$$

$$D_s = 1.143 \times 10^{-2} \cdot 2 = 2.29 \times 10^{-2} m$$

$$K = \frac{(2.29 \times 10^{-2})^2 0.65^2}{180(1 - 0.65)^2} = 2.5 \times 10^{-6} m^2$$

9.2. Appendix B

Heat transfer Co-efficient calculations using equation 4.26 and 4.27 (section 4):

First the Reynolds and Rayleigh numbers must be calculated to determine which equation is most suitable to use for the heat transfer co-efficient.

A Reynolds number higher than 10^5 indicate that equation 4.26 should be used, otherwise if less than, equation 4.27 is used.

Reynold's number:

$$Re_L = \frac{\rho U L}{\mu}$$

where,

ρ @ $600°C = 0.614 = density, kg\ m^{-3}$

$U = 1.2 =\ average\ velocity\ of\ gases, m\ s^{-1}$

$L = \frac{0.44\ m^3}{3.24\ m^2}\ characteristic\ lenght\ (Volume\ divided\ by\ surface\ area), m$

$\mu = 37.44 \times 10^{-6}\ Dynamic\ viscosity, Pa \cdot s$

$$Re_L = 2676 = 2.7 \times 10^3$$

A Re_L value of 2.7 x 10^3 < 10^5 therefore equation 4.26 should not be used to calculate heat transfer co-efficient.

$$Ra_L = \frac{\rho^2 g \Omega C_P \Delta T L^3}{\mu \kappa}$$

where,

$g = 9.81 = acceleration\ due\ to\ gravity, m\ s^{-2}$

$\Omega = 1.15 \times 10^{-3} = coefficient\ of\ thermal\ expansion, K^{-1}$

$C_P = 1.196 = Specific\ heat\ of\ capacity, kJ\ kg^{-1}K^{-1}$

$T = Temperature, K$

$\kappa = 61.8 \times 10^{-3} = heat\ conductivity\ of\ the\ gases\ @\ 600°C, 1\ atm., W\ m^{-1}K^{-1}$

$$Ra_L = 3207 = 3.2 \times 10^3$$

The Ra_L value of 3.2 x 10^3 ≤ 10^9 and therefore, equation 4.27 is used to calculate the heat transfer coefficient as shown below.

$$h = \frac{61.8 \times 10^{-3}}{0.136}\left(0.68 + \frac{0.67(3.2 \times 10^3)^{\frac{1}{4}}}{\left(1 + \left(\frac{0.492(61.8 \times 10^{-3})}{(37.44 \times 10^{-6})(1.196)}\right)^{\frac{9}{16}}\right)^{\frac{4}{9}}}\right)^2$$

$$h = 1.25\ W\ m^{-2}K^{-1}$$

9.3. Appendix C

Volume averaging method

The purpose of this appendix is to demonstrate how the conservation of momentum (section 4.3.2.) equations were derived over a porous medium using the volume averaging method.

Volume averaging of the microscopic conservation equation for convective heat transfer in a porous medium can be used to obtain the macroscopic conservation equation (Whitaker, 1967). Considering a porous medium with the phases; α and β, and $W_\alpha$is a quantity related to the α-phase, then an instrinsic phase average of $W_\alpha$is defined as:

$$W_\alpha = \frac{1}{V_\alpha}\int_{V_\alpha} W_\alpha \, dV \tag{A3.1}$$

when the volumetric integration is to be applied over $dV = dx'dy'dz'$ with (x', y', z') standing for the microscopic co-ordinates. The term V_α in equation A3.1 is the volume occupied by the α-phase in the total volume, V. Where $V = V_\alpha + V_\beta$, and $V_\beta$is the volume occupied by the β-phase.

Below (Equations A3.2a and A3.2b) are two averaging theorems obtained by Whitaker (1967) and Slattery (1967) and slightly modified by C. T. Hsu et al., (1990) to distinguish between the microscopic and macroscopic coordinates. They relate the volume average of a spatial derivative to the spatial derivative of a volume average and are used to aid the derivation of the macroscopic equations.

$$\frac{1}{V}\int_{V_\alpha} \nabla W_\alpha dV = \overline{\nabla}\left[\frac{1}{V}\int_{V_\alpha} W_\alpha dV\right] + \frac{1}{V}\int_{A_{\alpha\beta}} W_\alpha dS \tag{A3.2a}$$

$$\frac{1}{V}\int_{V_\alpha} \nabla \cdot \mathbf{W}_\alpha dV = \overline{\nabla} \cdot \left[\frac{1}{V}\int_{V_\alpha} \mathbf{W}_\alpha dV\right] + \frac{1}{V}\int_{A_{\alpha\beta}} \mathbf{W}_\alpha \cdot dS \quad \text{(A3.2b)}$$

where,

$A_{\alpha\beta}$= interface between the $\alpha$and β-phase in Volume, V

dS = surface vector

$W_\alpha and\ \mathbf{W}_\alpha$ = scalar and vector, respectively

∇ = gradient operator in the microscopic coordinates = $i\frac{\partial}{\partial x'} + j\frac{\partial}{\partial y'} + k\frac{\partial}{\partial z'}$

$\overline{\nabla}$ = gradient operator in the macroscopic coordinates = $i\frac{\partial}{\partial x} + j\frac{\partial}{\partial y} + k\frac{\partial}{\partial z}$

Overall Momentum equation derivation including drag forces for varying porosity medium

The equation A3.3 below describes the total volumetric drag force caused by solid particles that a fluid interacts with (flows past).

$$B = -\frac{1}{V}\int_{A_{fs}} \rho dS + \frac{\mu}{V}\int_{A_{fs}} (\nabla u) \cdot dS$$

where subscripts f and s are the fluid and solid phase quantities, respectively.

Taking the example of an array of spherical particles (for example) where the interaction between the fluid and solid is negligible. The body force term B can be written as follows:

$$B = \frac{ND^{(n)}}{V}$$

where the coefficient of the drag force,$D^{(n)}$ is:

$$D^{(n)} = -\int_{A_{fs}^{(n)}} p^{(n)}\, dS + \mu \int_{A_{fs}^{(n)}} \nabla u^{(n)} \cdot dS$$

and N is the number of sphere in volume, V. The terms $p^{(n)}$and $u^{(n)}$ are the local pressure and velocity in the flow field around the nth sphere, respectively. Assuming pseudo steady state, the momentum equation for $u^{(n)}$ becomes:

$$\rho\left(u^{(n)} \cdot \nabla\right)u^{(n)} = -\nabla p^{(n)} + \mu\nabla^2 u^{(n)}$$

By introducing the following dimensionless numbers, equation A3.6 becomes equation A3.7:

$$u^* = \frac{u^n}{|\bar{u}|}$$

$$p^* = \frac{p^n - \bar{p}}{p|\bar{u}|^2}$$

$$(x^*, y^*, z^*) = \left(\frac{x'}{d_p}, \frac{y'}{d_p}, \frac{z'}{d_p}\right)$$

where d_p is the diameter of the sphere, (m).

$$(u^* \cdot \nabla)u^* = -\nabla^* p^* + \frac{1}{Re_{fd}}\nabla^{*2} u^*$$

Where

$$Re_{fd} = \frac{|\bar{u}|d_p^2}{u}$$

At velocities larger than Re_{fd} (Local Reynolds number based on particle diameter and local average pore velocity) >> 10 there is viscous forces acting on the boundary of the spherical particle walls. Outside this layer the viscous forces become less important. The drag force coefficient is given as:

$$D^n = C_D \frac{d_p^2}{2}\rho|\bar{u}|^2 u^*$$

And

$$C_D = \frac{6\pi}{Re_{fd}^{\frac{1}{2}}}\left[c_o' + c_1' Re_{fd}^{\frac{1}{2}} + O\left(Re_{fd}^{-1}\right)\right]$$

With the zero order term coming as a result of skin friction and the first order correction accounting for form drag from the stagnation flow near the leading edge of the sphere.

For low Reynolds number flows the momentum equation is given as:

$$Re_{fd}(u^* \cdot \nabla^*)u^* = -\nabla^* p'^* + \nabla^{*2} u^*$$

and the drag coefficient, C_D for this flow regime is:

$$C_D = \frac{6\pi}{Re_{fd}}\left[c_o + c_1 Re_{fd} + O\left(Re_{fd}^2\right)\right]$$

And the zero order term accounting for Stokes drag and the first order is Oseen's correction.

From the above momentum equations for large and small Reynolds number flows, it can be concluded that at low Reynolds numbers, the drag coefficient (A3.11) is dominated by $\frac{6\pi c_o}{Re_{fd}}$, associated with the Stokes drag and $6\pi c_1$ is the inertial force correction. High Reynold number flows equation (A3.9) shows that if flow is increased ten the skin friction of the laminar boundary larger dominates with a coefficient of $\frac{6\pi c_o'}{Re_{fd}^{\frac{1}{2}}}$, meanwhile the stokes drag is degenerated to a stagnation form near the leading edge of the sphere. If increased further, the flow will likely separate from the surface of the sphere to form a wake. The inertial effect of the flow pre-dominates the drag forces associated with the wake with a constant drag force:

$$C_D = 6\pi c_o''$$

Combining the drag coefficents (A3.9, A3.11 and A3.12), the drag coefficient can be presented as:

$$C_D = 6\pi\left(\frac{\frac{c_o}{Re_{fd} + c_o'}}{Re_{fd}^{\frac{1}{2}} + c_o''}\right)$$

subbing equation A3.8 and A3.13 into A3.4 produces:

$$B = -\frac{18(1-\varphi)}{d_p^2}\left[c_o + c_o' Re_{fd}^{\frac{1}{2}} + c_o'' Re_{fd}\right]\mu_f|\bar{u}|u^*$$

where

$$\frac{4\pi R^3 N}{3V} = 1 - \emptyset$$

and R is the radius of the sphere, (m). The term $\emptyset$ is the porosity of the packed bed, (-), and the three constants, c_o, c_o', and c_o'' are:

$$c_o = \frac{a(1-\varphi)}{18\emptyset}$$

$$c_o' = 0$$

$$c_o'' = \frac{b}{18}$$

And thus this equation (3.14) can be reduced to:

$$B = -\left[\frac{\mu\varphi u}{K} + \rho\frac{F\varphi u|u|}{\sqrt{K}}\right]$$

where

$u = \emptyset\bar{u} = Darcy\ velocity, ms^{-1}$

$$K = \frac{\varphi^3 d_p^2}{a(1-\varphi)^2}$$
$$= Permeability\ as\ defined\ by\ the\ Carmen - Kozeny\ equation\ (Appendix\ A)$$

$$F = \frac{b}{\sqrt{a\varphi^{\frac{3}{2}}}}$$

where a and b are the Ergun constants:

$$a = \frac{150}{b} + 1.75$$

$$a = \frac{\Delta P}{L}\frac{D_p}{\rho u^2}\left(\frac{\varphi}{1-\varphi}\right)$$

$$b = \frac{\rho u D_p}{(1-\varphi)\mu}$$

where,

L = length of the packed bed, (m)

D_P = equivalent spherical diameter of the bed, (m)

ρ = density of fluid, (kg m^{-3})

φ = porosity of the packed bed, (-)

μ = dynamic viscosity of the fluid, (Pa.s)

ΔP = pressure drop across the bed, (Pa)

Therefore, the overall macroscopic momentum equation for an incompressible fluid in a variable porosity medium is given as:

$$\rho\left[\frac{\partial u}{\partial t}+\overline{\nabla}\cdot\left(\frac{u^2}{\varphi}\right)\right]=-\overline{\nabla}p+\mu\overline{\nabla}^2u-\left[\frac{\mu\varphi u}{K}+\rho\frac{F\varphi u|u|}{\sqrt{K}}\right]$$

9.4. Appendix D

Experimental data as shown in section 6.1, figure 6-1 was collected during a pyrolysis run. Thermocouples were placed in the centre of the reactor (Perforated core) and in the bottom of the flue stack. The reactor was filled with 70 kg of air dried (<5% MC) wood chips. Heat was supplied by the burners in the combustion chamber and the temperature readings of the thermocouples were recorded over time. This was the only parameter monitored in the reactor and thus was used to verify the model.